Supporting Information

Unleashing Non-Conjugated Polymer as Charge Relay Mediator

Table of Contents

Page NO.

Experimental Section

1. Materials

Zinc acetate dehydrate [$Zn(CH_3COO)_2 \cdot 2H_2O$], cadmium acetate dihydrate [$Cd(CH_3COO)_2 \cdot 2H_2O$], thioacetamide (TAA), Anhydrous Sodium Sulfite (Na_2SO_3), Hydrofluoric acid (HF), ammonium hydroxide ($NH_3 \cdot H_2O$), silver nitrate ($AgNO_3$), Methanol (CH_3OH), Ethanol (C_2H_6O), Ethylene glycol ($C_2H_6O_2$), Glycerol ($C_3H_8O_3$), Lactic acid ($C_3H_6O_3$), cadmium chloride hemi(pentahydrate) ($CdCl_2 \cdot 2.5H_2O$), S powder, 2-aminoethanethiol (AET) and 3-aminopropyl-trimethoxysilane ($C_9H_{23}NO_3Si$, APTES) were obtained from Sinopharm Chemical Reagent Co., Ltd. (Shanghai, China). Sodium sulfide ($Na_2S \cdot 9H_2O$), Indium chloride ($InCl_3$), 4-Nitroaniline (4-NA), 2-nitroaniline(2-NA), 4-nitrophenol, 2-nitrophenol, 1-Bromo-4-Nitrobenzene, 1-chloro-4-nitrobenzene, 4-nitrotoluene and 4-nitroanisole were obtained from Aladdin Industrial Corporation (Shanghai, China). Branched Polyethylenimine (BPEI), Poly(dimethyldiallylammonium) chloride (PDDA) and Poly(allylamine hydrochloride) (PAH) were obtained from Sigma-Aldrich (China) Co., Ltd. Deionized water (DI H_2O, Millipore,18.2 MΩ·cm resistivity). Ti_3AlC_2 was purchased from Laizhou Kai Kai Ceramic Materials Co., Ltd. All the materials are analytical grade and used as received without further purification.

2. Preparation of $ZnIn_2S_4$ nanosheets[S1]

Single-unit-cell $ZnIn_2S_4$ layers were fabricated by a facile low-temperature refluxing method. In detail, 1.5 mmol of $Zn(CH_3COO)_2 \cdot 2H_2O$ and 3 mmol of $InCl_3$ were added into 250 mL DI water and stirred for 30 min. Subsequently, an excess amount of thioacetamide (TAA, 8 mmol) was added into the above solution and stirred for another 30 min. The solution was then heated to 95℃ and maintained at that temperature for 5 h under vigorous stirring. After cooling to room temperature, the $ZnIn_2S_4$ (ZIS) precipitate was collected by centrifugation and washed with DI H_2O three times.

3. Preparation of CdS nanosheets[S2]

CdS nanosheets were prepared via a hydrothermal method reported previously. In detail, 0.32 mmol $CdCl_2 \cdot 2.5H_2O$, 2.0 mmol S powder and 12 mL of diethylenetriamine (DETA) were mixed and

vigorously stirred to form a homogeneous suspension. Then, the mixture was transfer into a Teflon-lined stainless-steel autoclave with a capacity of 50 mL for 48 h at 80 °C. After cooling to room temperature, a yellowish precipitate was rinsed with deionized water and ethanol separately and dried in an oven at 60 °C for 24 h to obtain the CdS nanosheets.

4. Preparation of $CdIn_2S_4$ nanosheets[S1]

$CdIn_2S_4$ nanosheets were fabricated by a facile low-temperature refluxing method. In detail, 1.5 mmol of $Cd(CH_3COO)_2 \cdot 2H_2O$ and 3 mmol of $InCl_3$ were added into 250 mL DI water and stirred for 30 min. Subsequently, an excess amount of thioacetamide (TAA, 8 mmol) was added into the above solution and stirred for another 30 min. The solution was then heated to 100℃ and maintained at that temperature for 12 h under vigorous stirring. After cooling to room temperature, the $CdIn_2S_4$ precipitate was collected by centrifugation and washed with DI H_2O three times.

5. Preparation of In_2S_3 nanosheets[S3]

In_2S_3 nanosheets were fabricated by a facile low-temperature refluxing method. In detail, 8 mmol of TAA and 3 mmol of $InCl_3$ were added into 250 mL DI water and stirred for 30 min. The solution was then heated to 95℃ and maintained at that temperature for 5 h under vigorous stirring. After cooling to room temperature, the In_2S_3 precipitate was collected by centrifugation and washed with DI H_2O three times.

6. Preparation of Ti_3C_2 QDs (MXene QDs)[S4]

Ti_3AlC_2 (2.0 g) powder was immersed in 40 mL 48% HF and stirred for 20 h at 60 °C. The obtained powder was then rinsed multiple times with deionized water. The powder pellet was retrieved by centrifugation at 3500 rpm for 10 min, and the supernatant was discarded. The final product (Ti_3C_2 powder) was dried at 60 °C under vacuum for 12 h. In an N_2–protected environment, the Ti_3C_2 powder was then placed in 80 mL deionized water followed ultrasound for 1h. The pH of mixer was adjusted around 9 by ammonia and the mixer was transferred into 75 mL Teflon-lined stainless steel autoclave at 120 °C and for 6 h. The MQDs could be obtained by filtering the mixture by 220 nm membrane.

7. Preparation of $ZnIn_2S_4$/MQDs (ZM) nanocomposites

ZIS NSs (100 mg) were added into 10 mL of MQDs aqueous solution (25 ppm, pH = 9), stirred for 1 hour, ZM was collected by centrifugation, and dried in vacuum at 333K for 12 h.

8. Preparation of ZIS/polymers binary nanocomposites

ZIS NSs (100 mg) were added into 10 mL of polymers solution (10 mg/mL), and vigorously stirred for 1 hour. After that, the mixture was centrifuged, and the thus-obtained polymers-modified ZIS were thoroughly washed with deionized (DI) H_2O to remove residual free polymers adsorbed on the surface. Finally, the obtained powder was dried in vacuum at 333K for 12 hours. (polymers: poly(dimethyldiallylammonium) chloride (PDDA), branched polyethylenimine (BPEI), poly(allylamine hydrochloride) (PAH), 2-aminoethanethiol (AET) and 3-aminopropyl-trimethoxysilane (APTES).)

9. Preparation of ZIS/polymers/MQDs ternary nanocomposites

ZIS/polymers/MQDs nanocomposites were fabricated via an electrostatic self-assembly method under ambient conditions. In detail, ZIS/polymers (100 mg) were added into 10 mL of MQDs aqueous solution (25 ppm, pH = 9), stirred for 1 hour, washed with DI H_2O, and dried in vacuum at 333K for 12 hours, resulting in the ZIS/polymers/MQDs ternary nanocomposites

10. Fabrication of the working electrodes in PEC measurement

The working electrode was prepared on fluorine-doped tin oxide (FTO) glass that was cleaned by sonication in ethanol for 30 min and dried at 313 K. The boundary of FTO glass was protected using Scotch tape. Next, 5 mg of the sample was dispersed in 0.5 mL of ethanol by sonication to get a slurry, which was spread onto the pretreated FTO glass. After air-drying, remove the Scotch tape. The exposed area of the working electrode was 1 cm^2. Finally, the working electrode was vertically dipped into the electrolyte and irradiated with visible light ($\lambda > 420$ nm) (PLS-SXE300D, Beijing Perfect Light Co. Ltd, China).

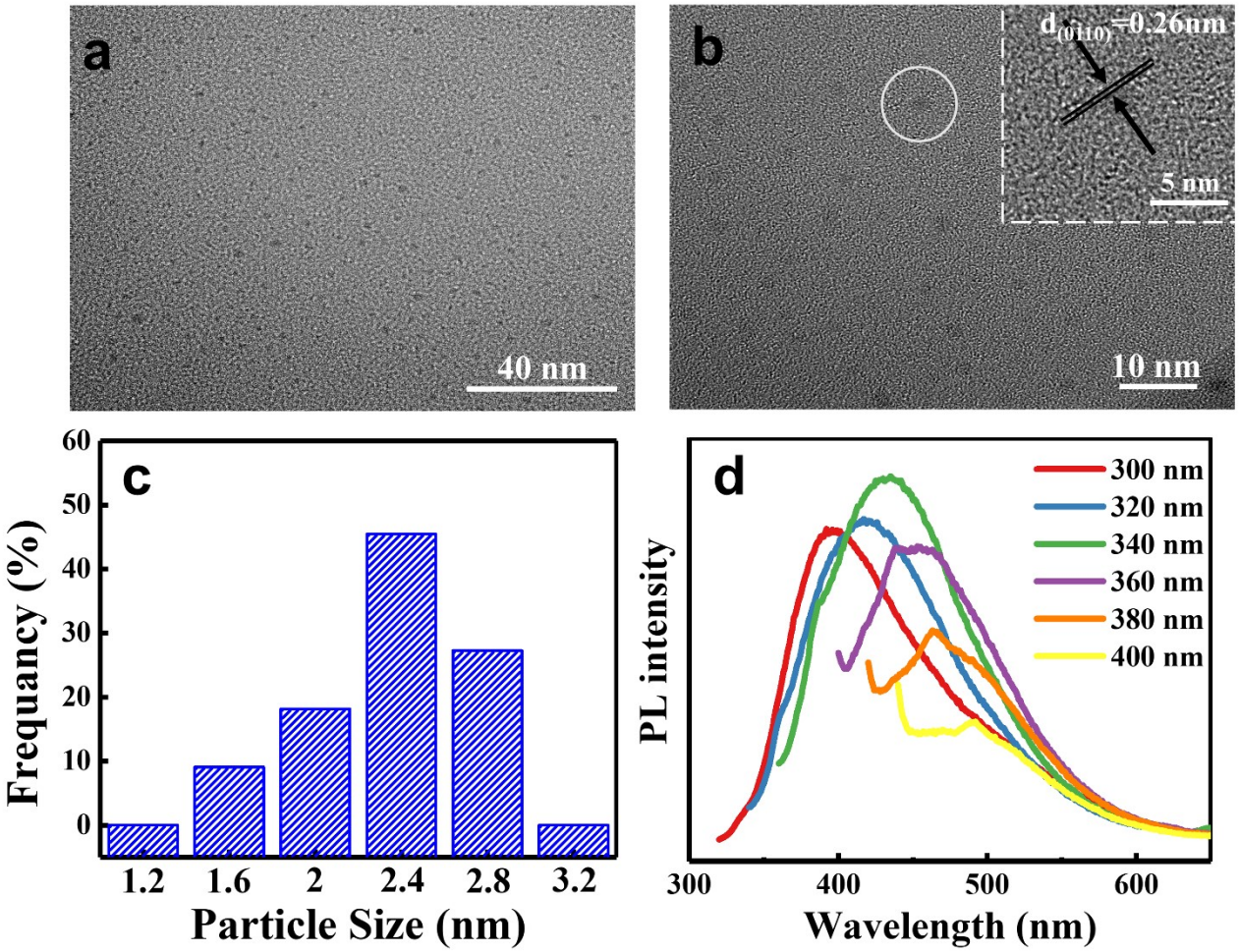

Fig. S1. (a) Low-magnified and (b) HRTEM images of MQDs. (c) Size distribution histogram of MQDs obtained from TEM image. (d) PL spectra of MQDs under different excitation wavelengths.

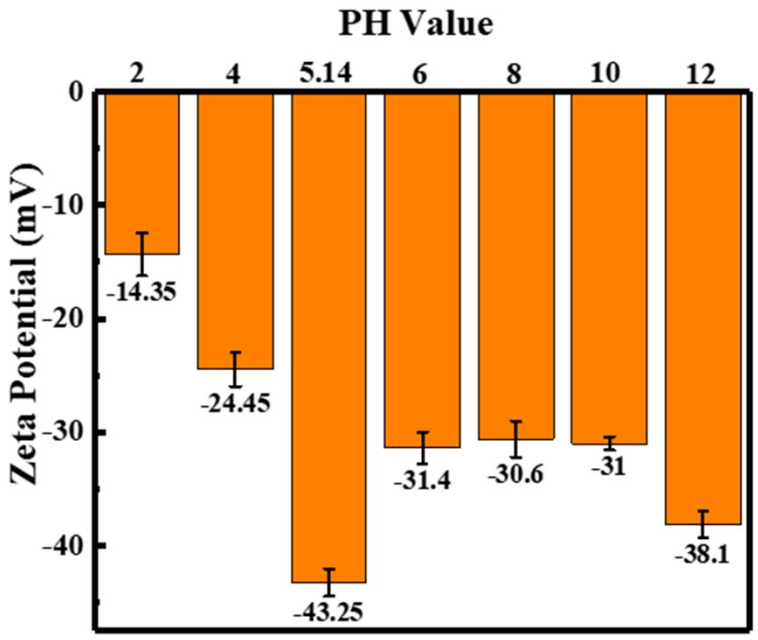

Fig. S2. Zeta potentials of ZIS NSs.

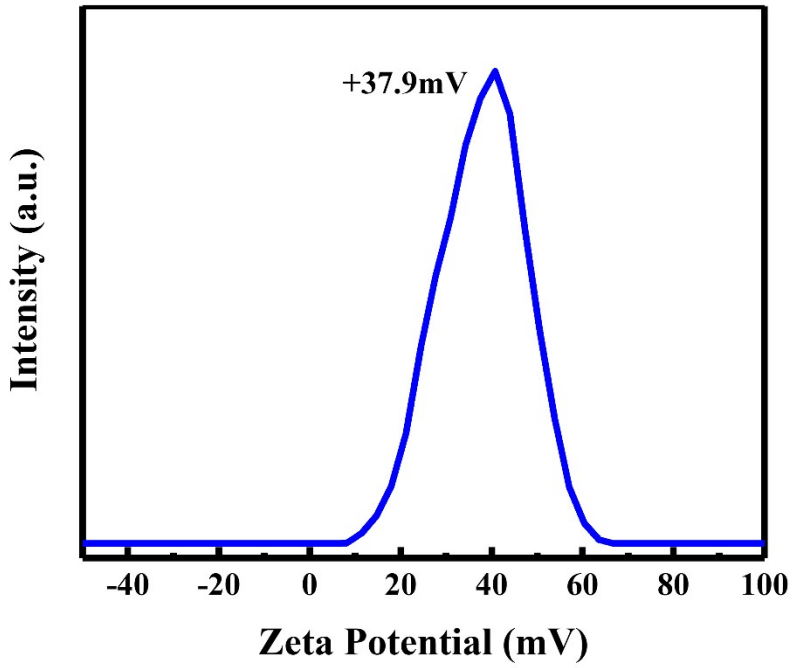

Fig. S3. Zeta potentials of ZP.

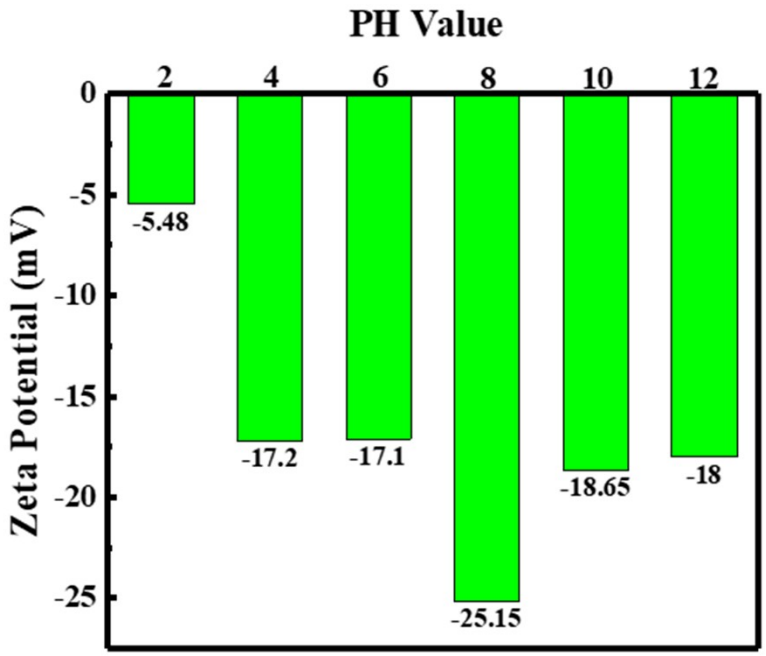

Fig. S4. Zeta potentials (ξ) of MQDs.

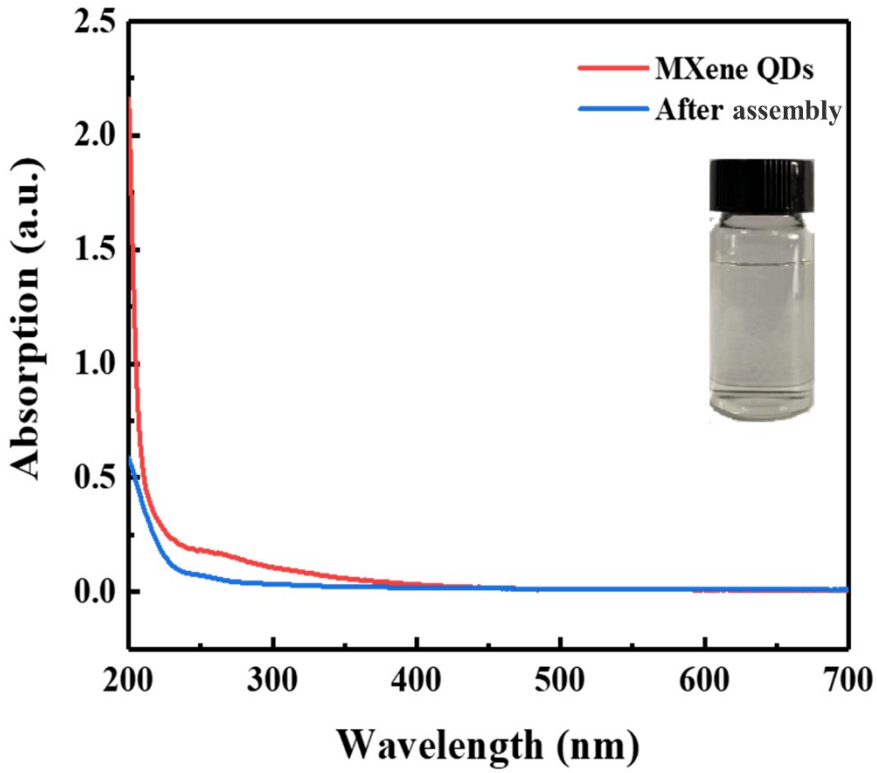

Fig. S5. UV-vis absorption spectra of pristine MQDs and supernatant after mixing with ZP. The inset shows the graph of colloidal MQDs aqueous solution.

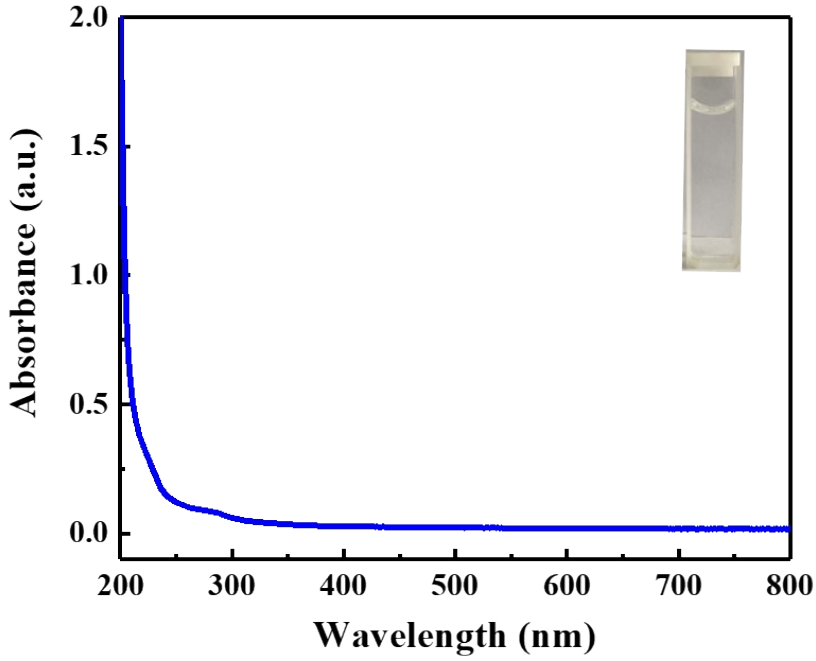

Fig. S6. UV-vis absorption spectrum of PDDA aqueous solution.

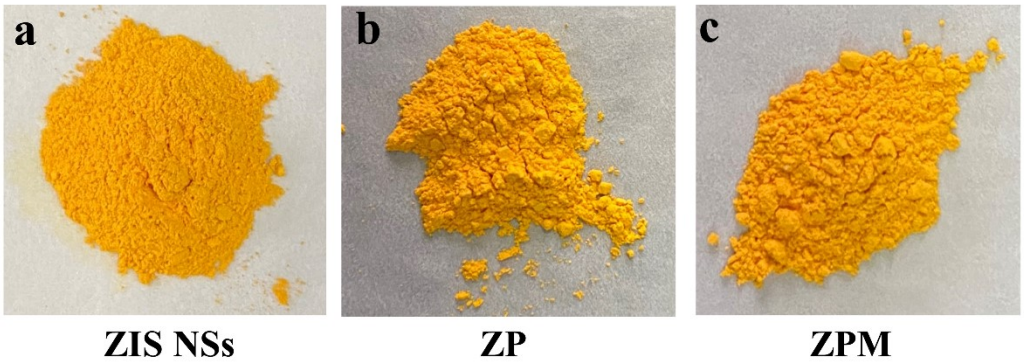

Fig. S7. Sample colors of (a) ZIS NSs, (b) ZP and (c) ZPM.

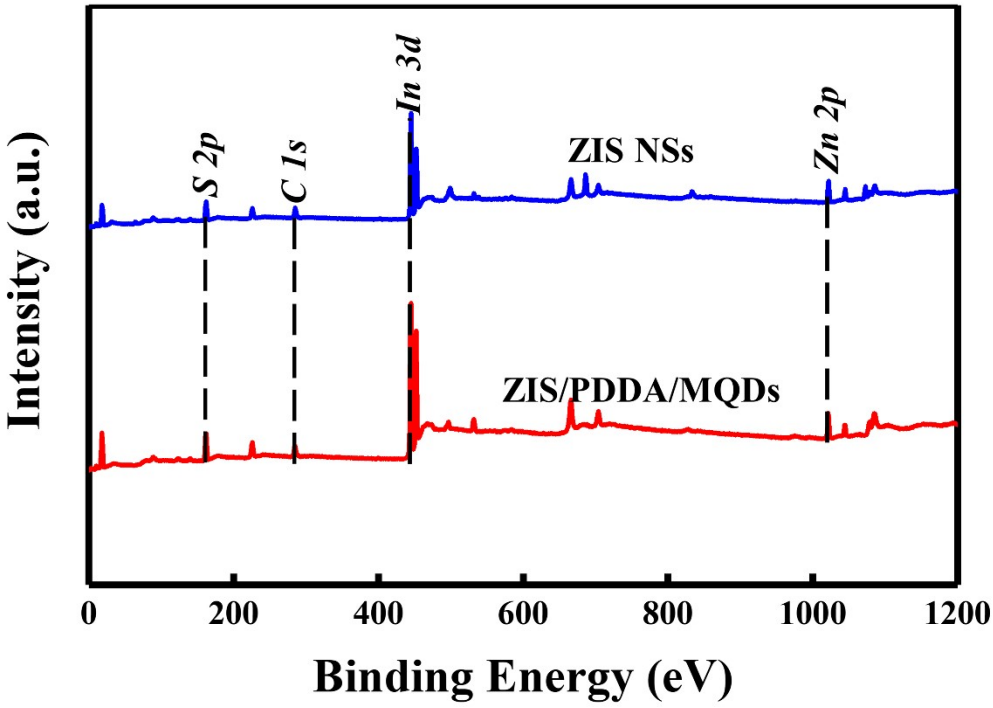

Fig. S8. Survey spectra of ZIS and ZPM.

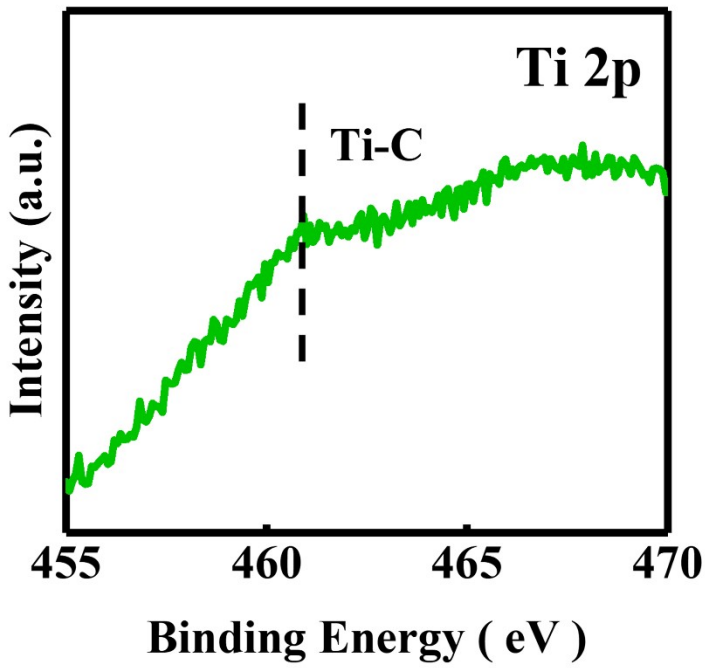

Fig. S9. High-resolution Ti 2p spectrum of ZPM.

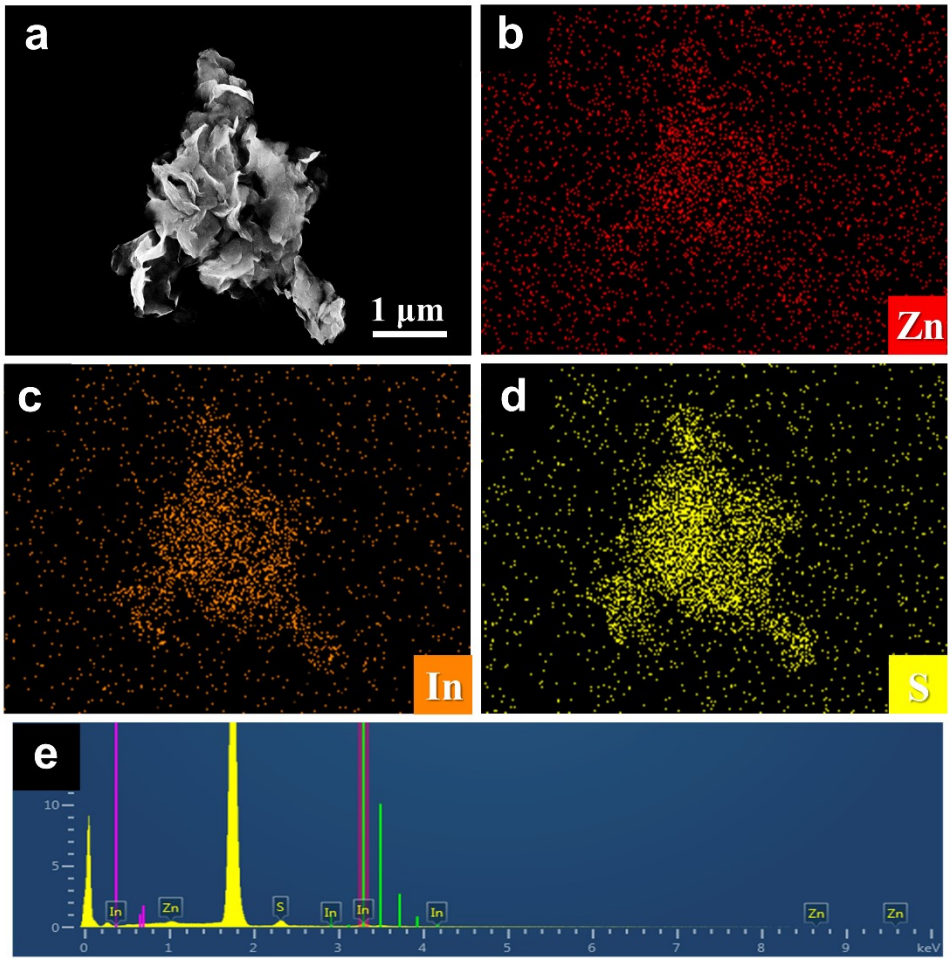

Fig. S10. FESEM image (a) and low-magnified FESEM image of ZIS NSs with (b-d) elemental mapping and (e) EDS results.

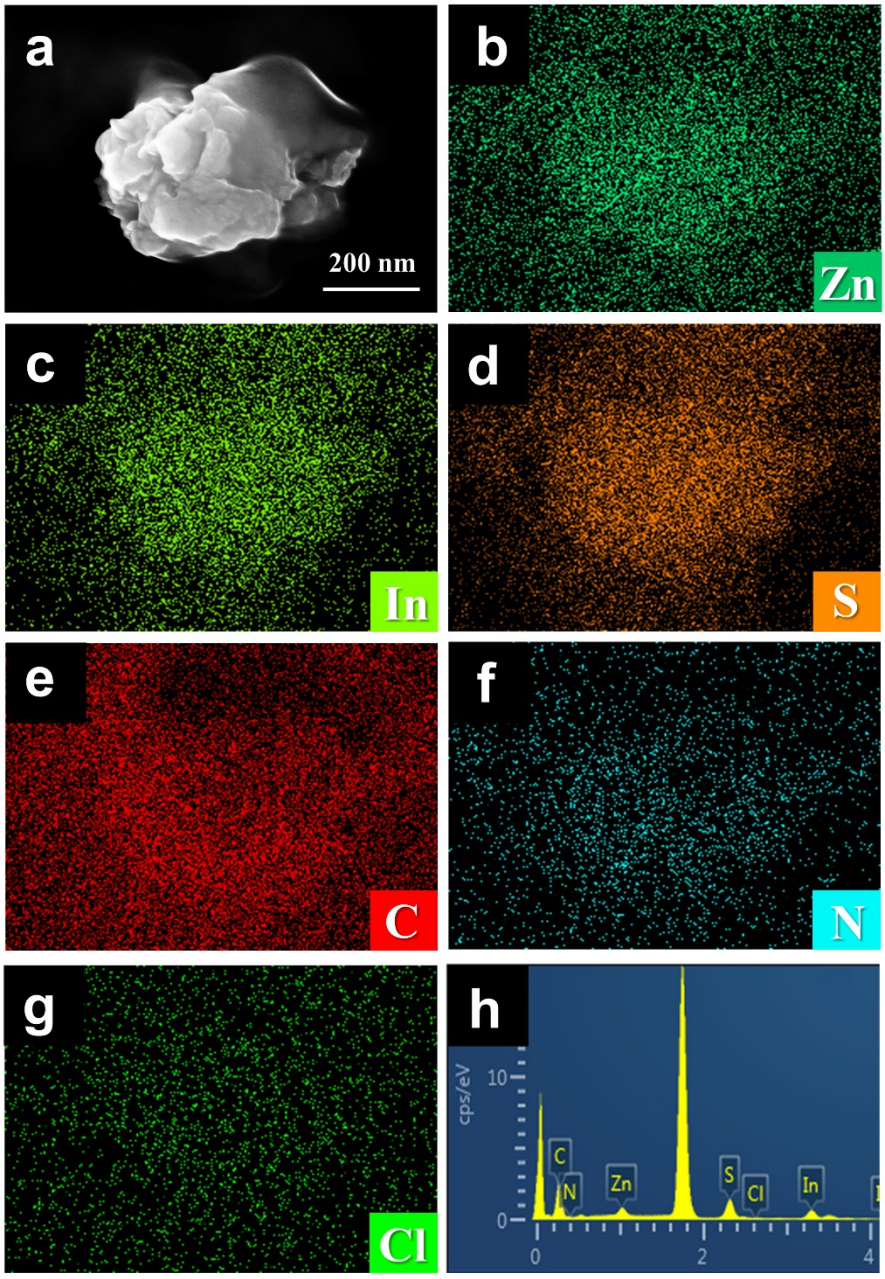

Fig. S11. FESEM image (a) and low-magnified FESEM image of ZP with (b-g) elemental mapping and (h) EDS results.

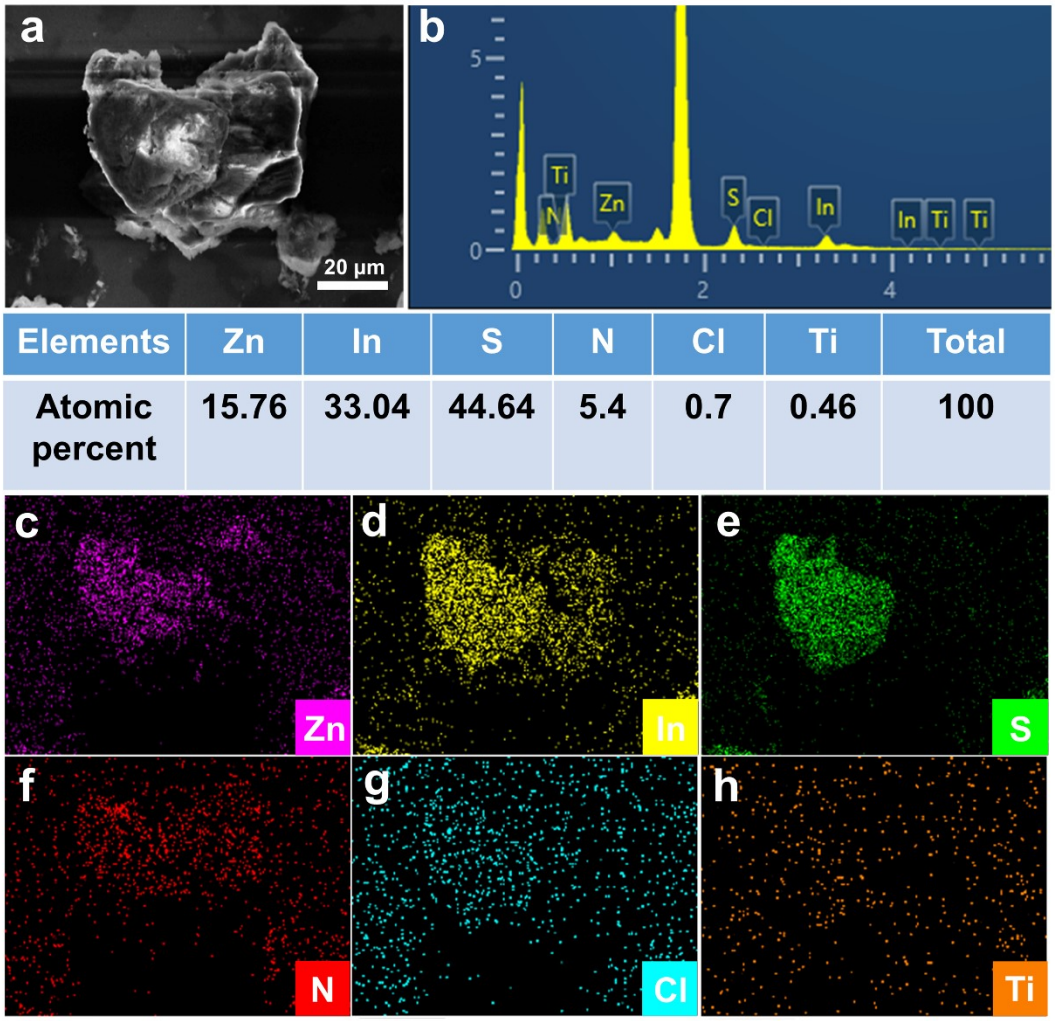

Elements	Zn	In	S	N	Cl	Ti	Total
Atomic percent	15.76	33.04	44.64	5.4	0.7	0.46	100

Fig. S12. (a) FESEM image of ZPM with (c-h) elemental mapping and (b) EDS results.

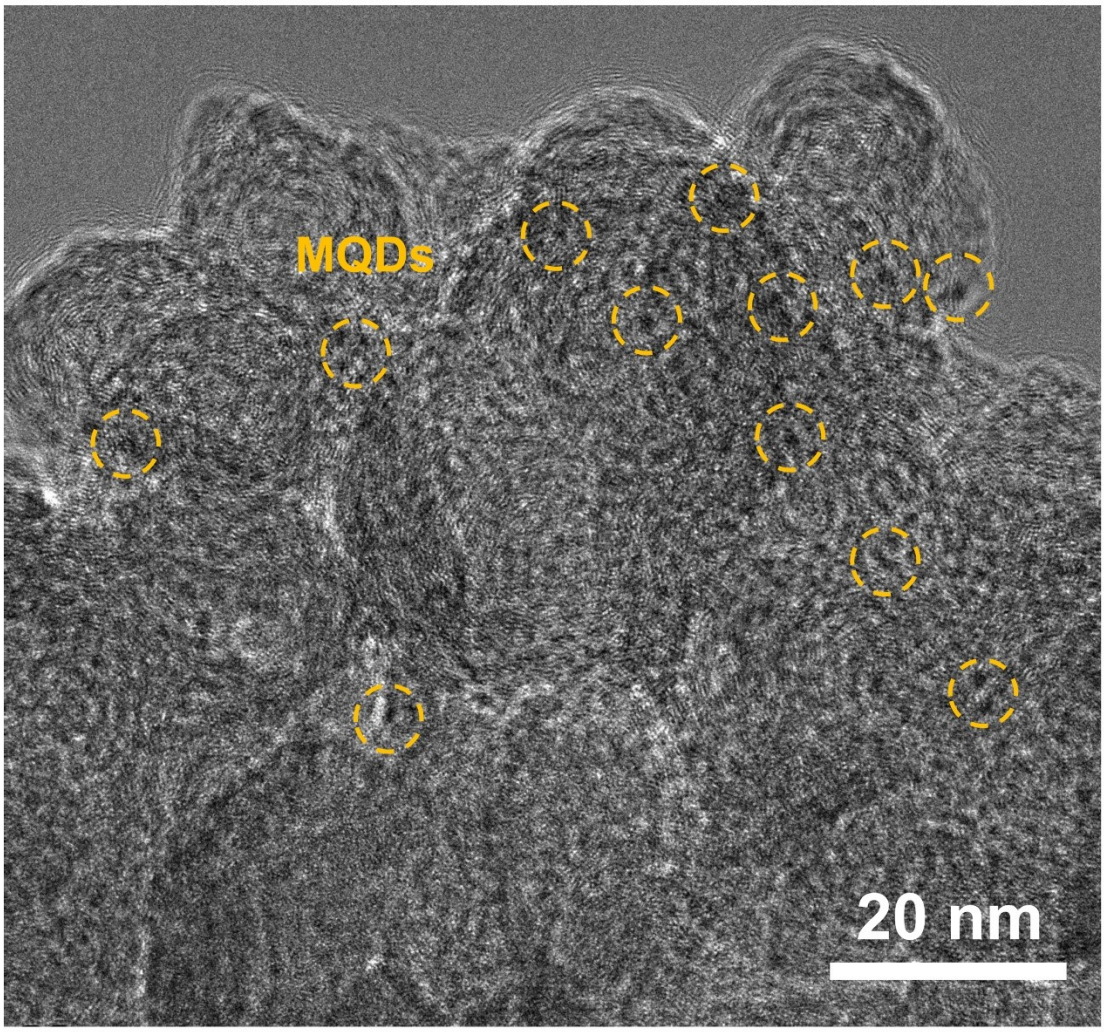

Fig. S13. HRTEM image of ZPM.

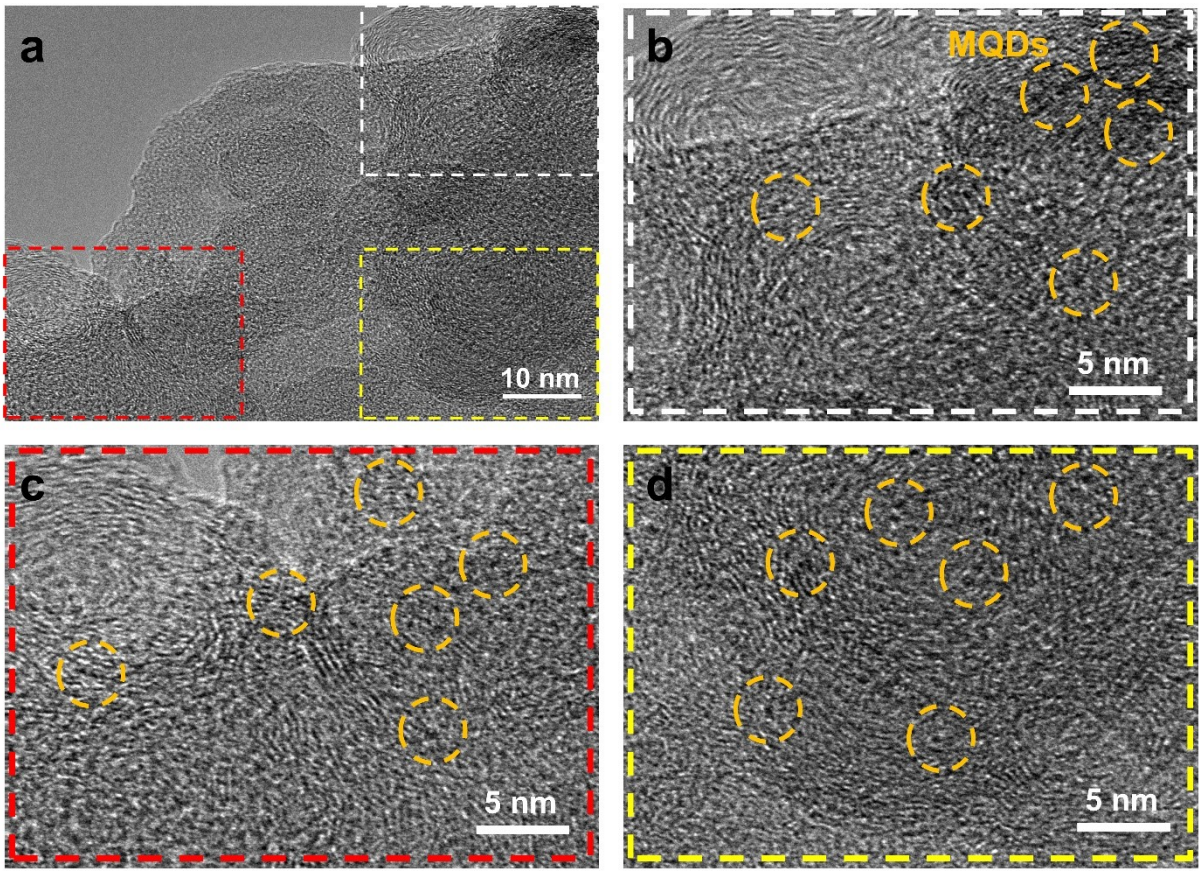

Fig. S14. Magnified TEM images of ZPM.

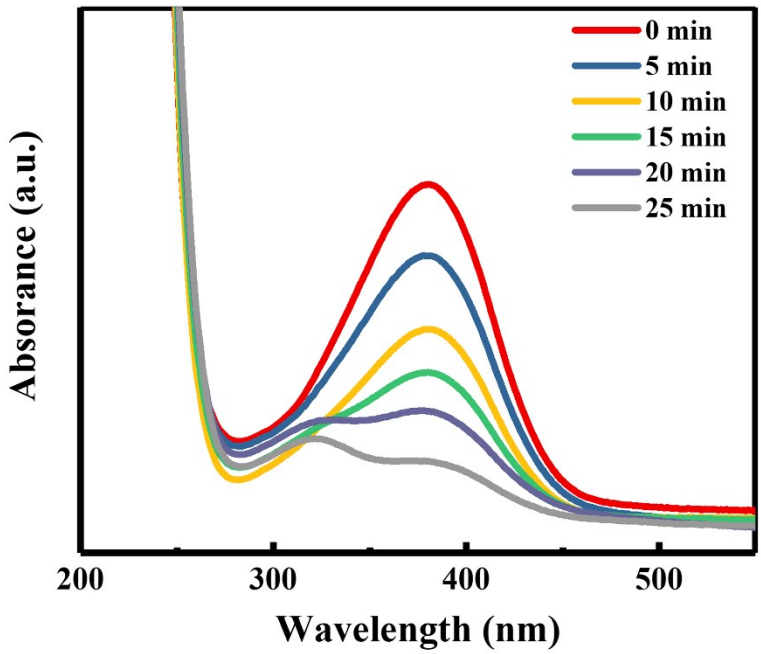

Fig. S15. UV-vis absorption spectra of 4-NA collected after designated irradiation time (25 min) when it was reduced over ZPM under visible light irradiation (λ>420 nm) with the addition of Na_2SO_3 as hole quencher and N_2 purge under ambient conditions.

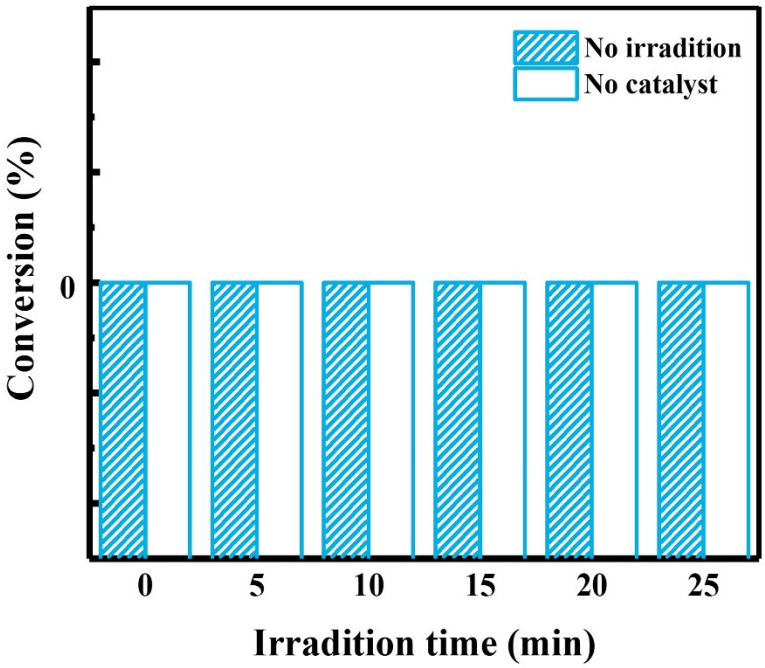

Fig. S16. Photoactivities of ZPM toward 4-NA photoreduction without adding catalyst or light irradiation.

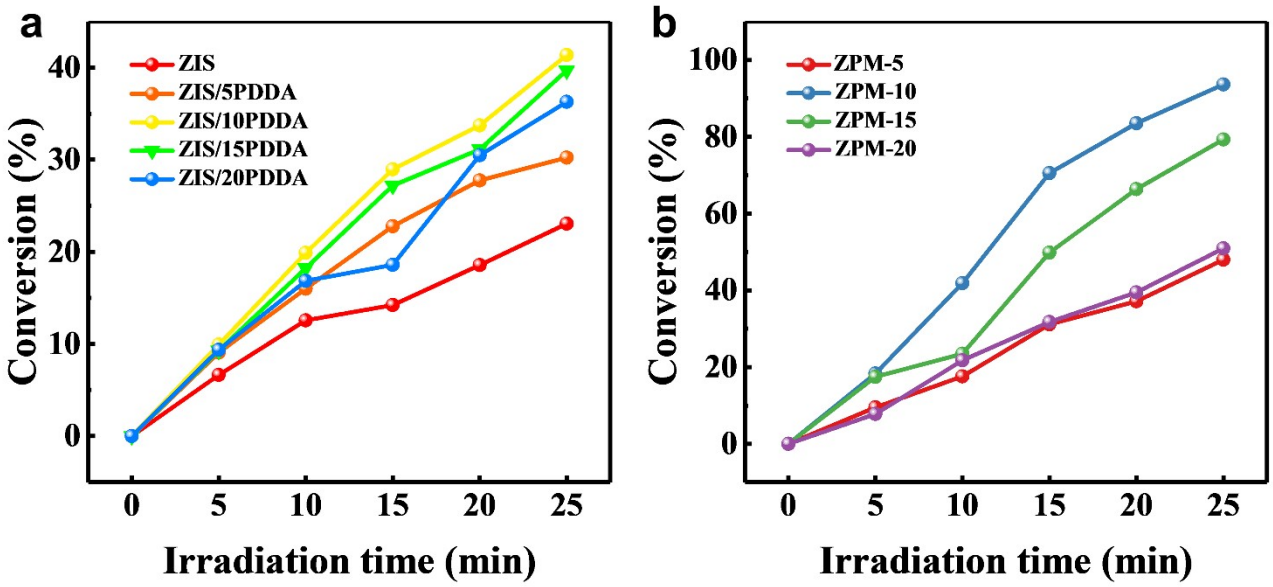

Fig. S17. (a) Photoactivities of ZP with different PDDA concentration (5, 10, 15, 20 mg/mL) toward anaerobic reduction of 4-NA to 4-PDA under visible light irradiation (λ > 420 nm) and (b) photoactivities of ZPM with different adding volume of MQDs colloidal solution (5, 10, 15, 20 mL) under the same conditions.

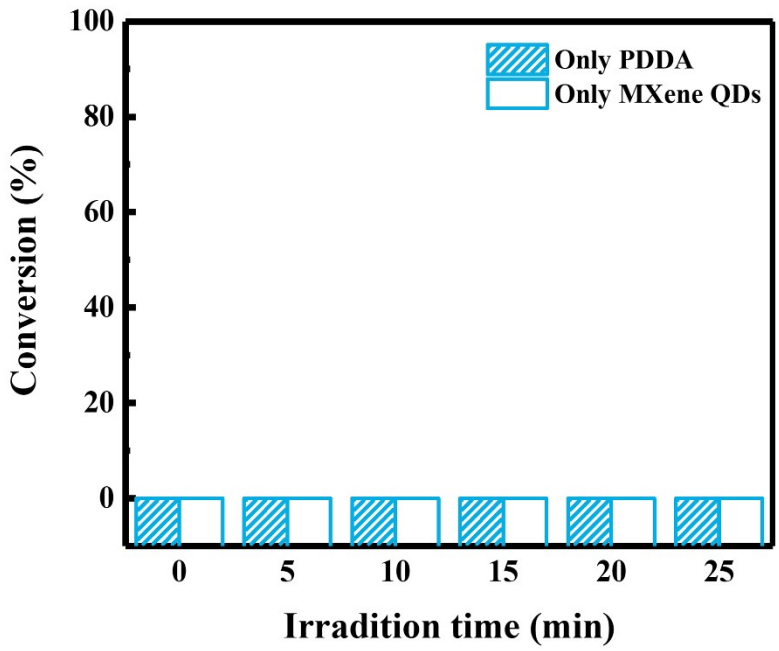

Fig. S18. Photoactivities of PDDA and MQDs toward 4-NA reduction.

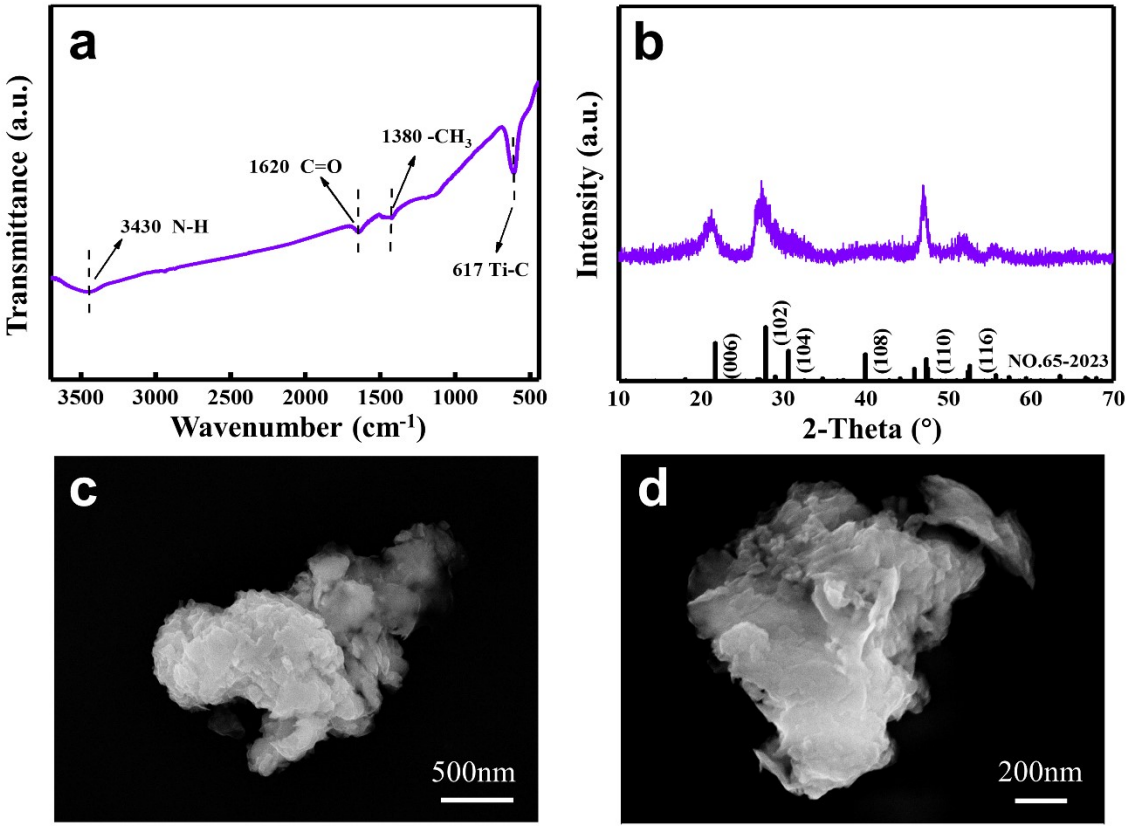

Fig. S19. (a) FTIR spectra, (b) XRD pattern, (c) and (d) FESEM image of ZM.

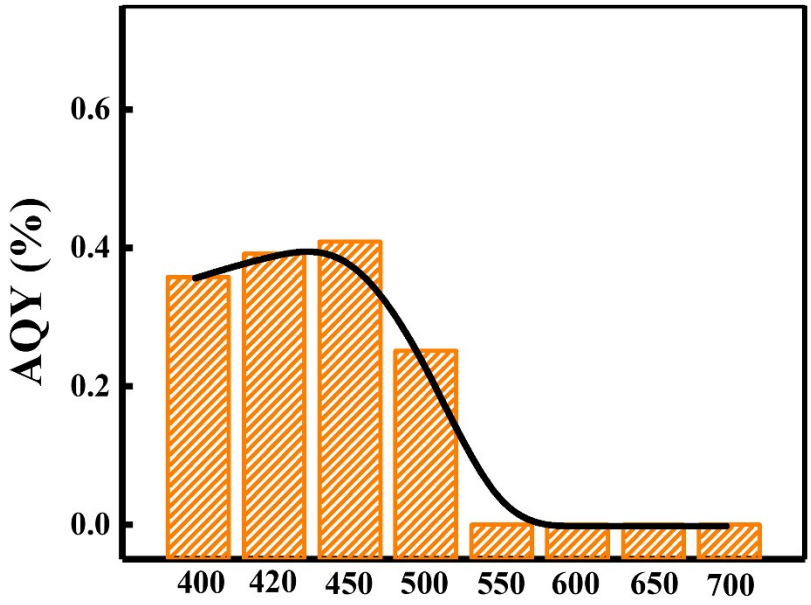

Fig. S20. A.Q.Y. of ZPM under monochromatic light irradiation.

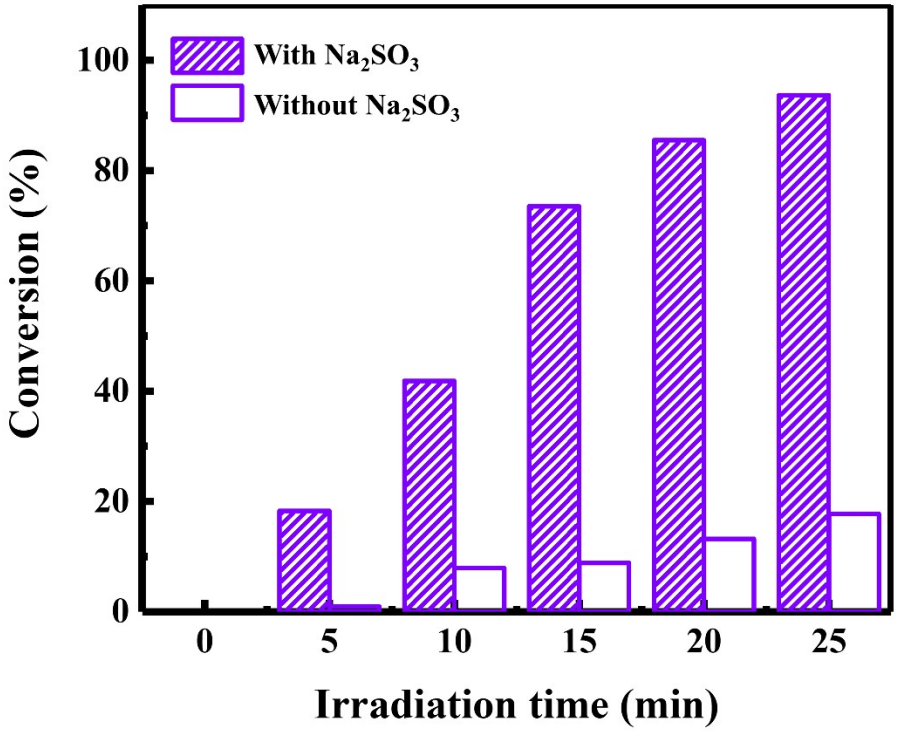

Fig. S21. Photoactivities of ZPM with and without adding Na_2SO_3 toward 4-NA photoreduction.

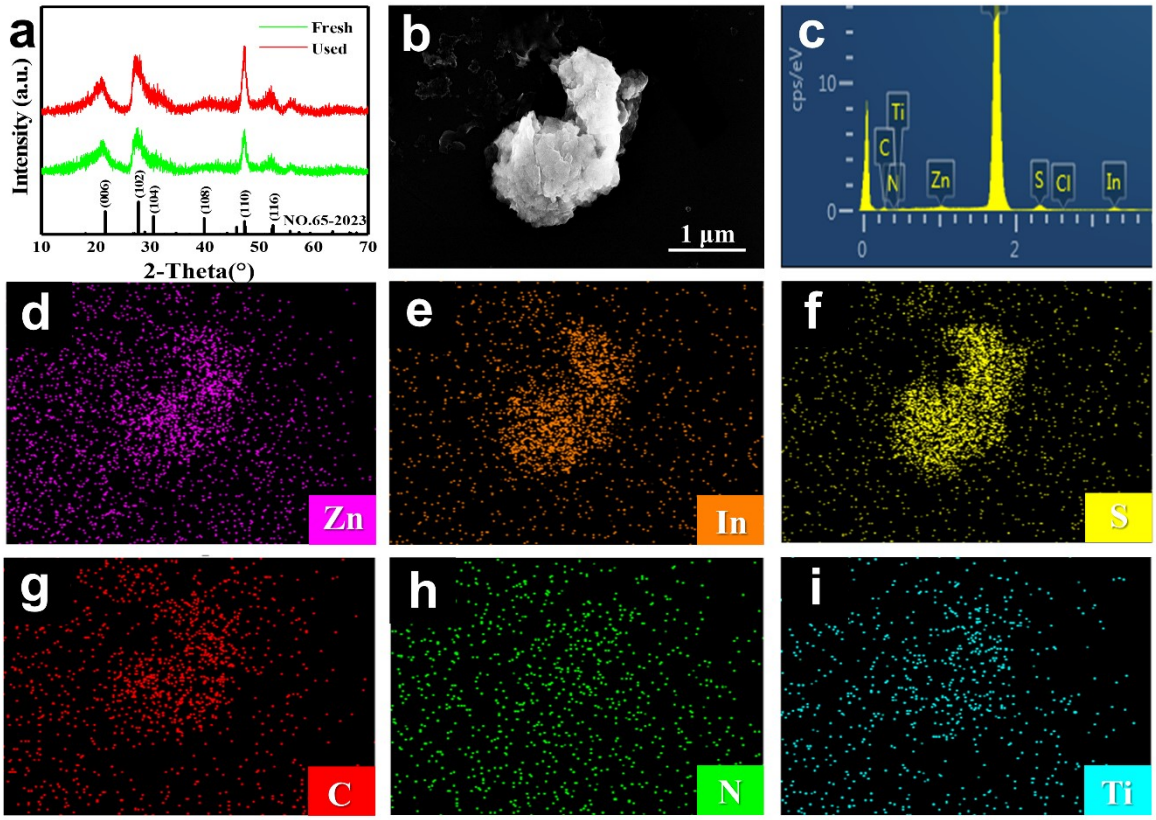

Fig. S22. (a) XRD pattern, (b) FESEM image and (c) EDS result of ZPM after cyclic reactions with (d-i) elemental mapping results.

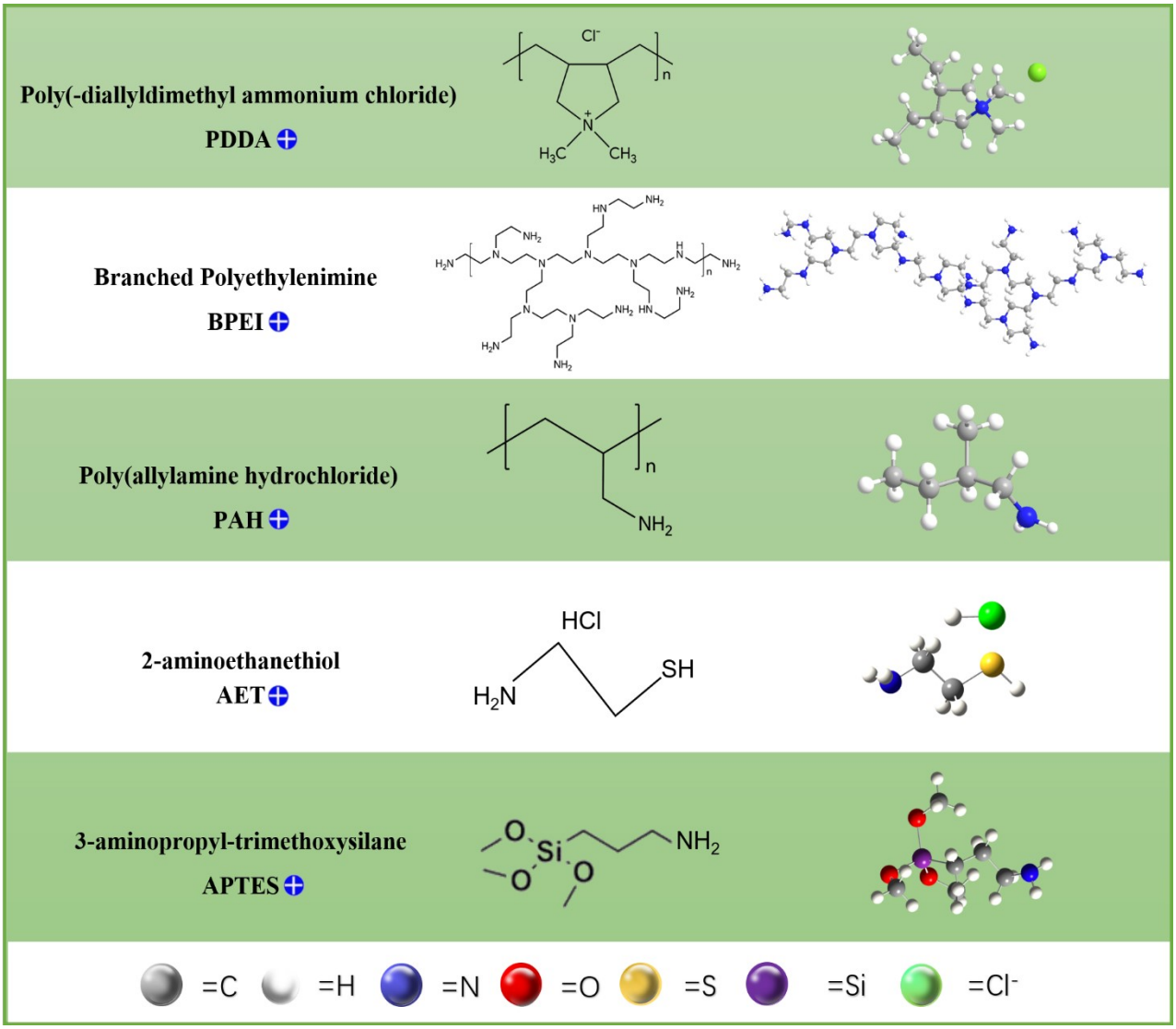

Fig. S23. Molecular structures of different polyelectrolytes or molecules.

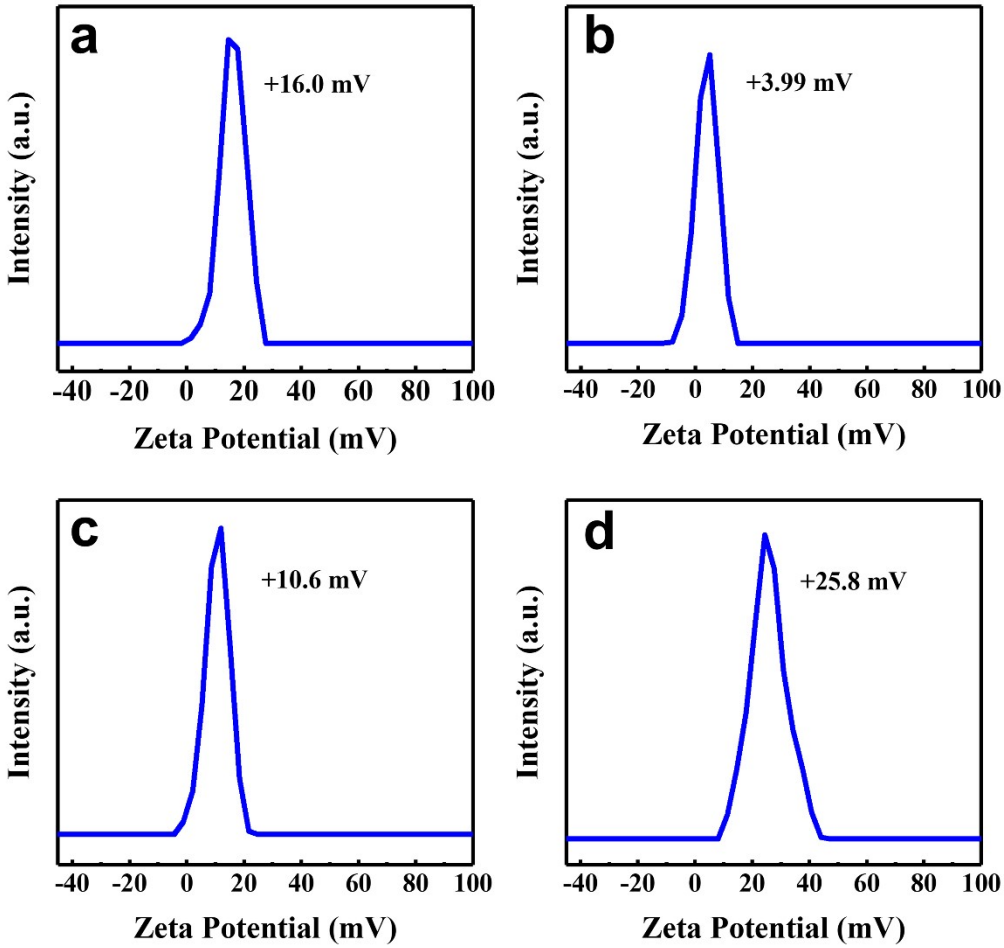

Fig. S24. Zeta potentials (ξ) of (a) ZIS/BPEI, (b) ZIS/PAH, (c) ZIS/AET and (d) ZIS/APTES.

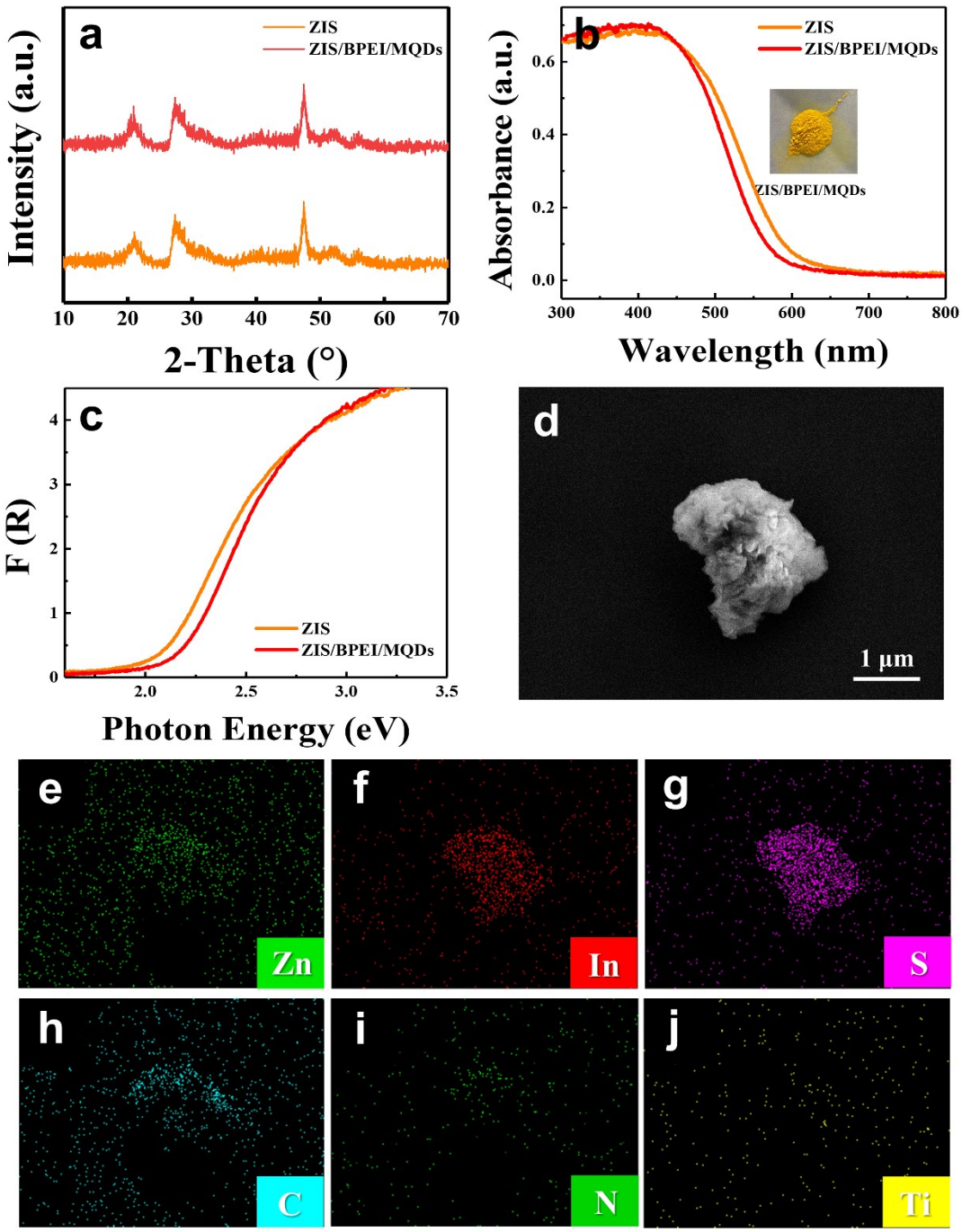

Fig. S25. (a) XRD patterns of blank ZIS and ZIS/BPEI/MQDs; (b) DRS spectra of ZIS and ZIS/BPEI/MQDs with (c) transformed plots calculated based on the Kubelka–Munk function vs. the energy of light; (d) FESEM image and (e-j) elemental mapping result of ZIS/BPEI/MQDs.

Note: XRD pattern of ZIS/BPEI/MQDs (**Fig. S25a**) shows the hexagonal phase $ZnIn_2S_4$ (JCPDS No. 65-2023) [S1], similar to that of pure $ZnIn_2S_4$. As displayed in **Fig. S25(b & c)**, $ZnIn_2S_4$ and ZIS/BPEI/MQDs exhibit the similar absorption edge, indicating both BPEI and MQDs deposition does not influence the optical property of $ZnIn_2S_4$ NSs. Elemental mapping result of ZIS/BPEI/MQDs in **Fig. S25(e-j)** demonstrates the uniform distribution patterns of Zn, In, S, C, N and Ti signals.

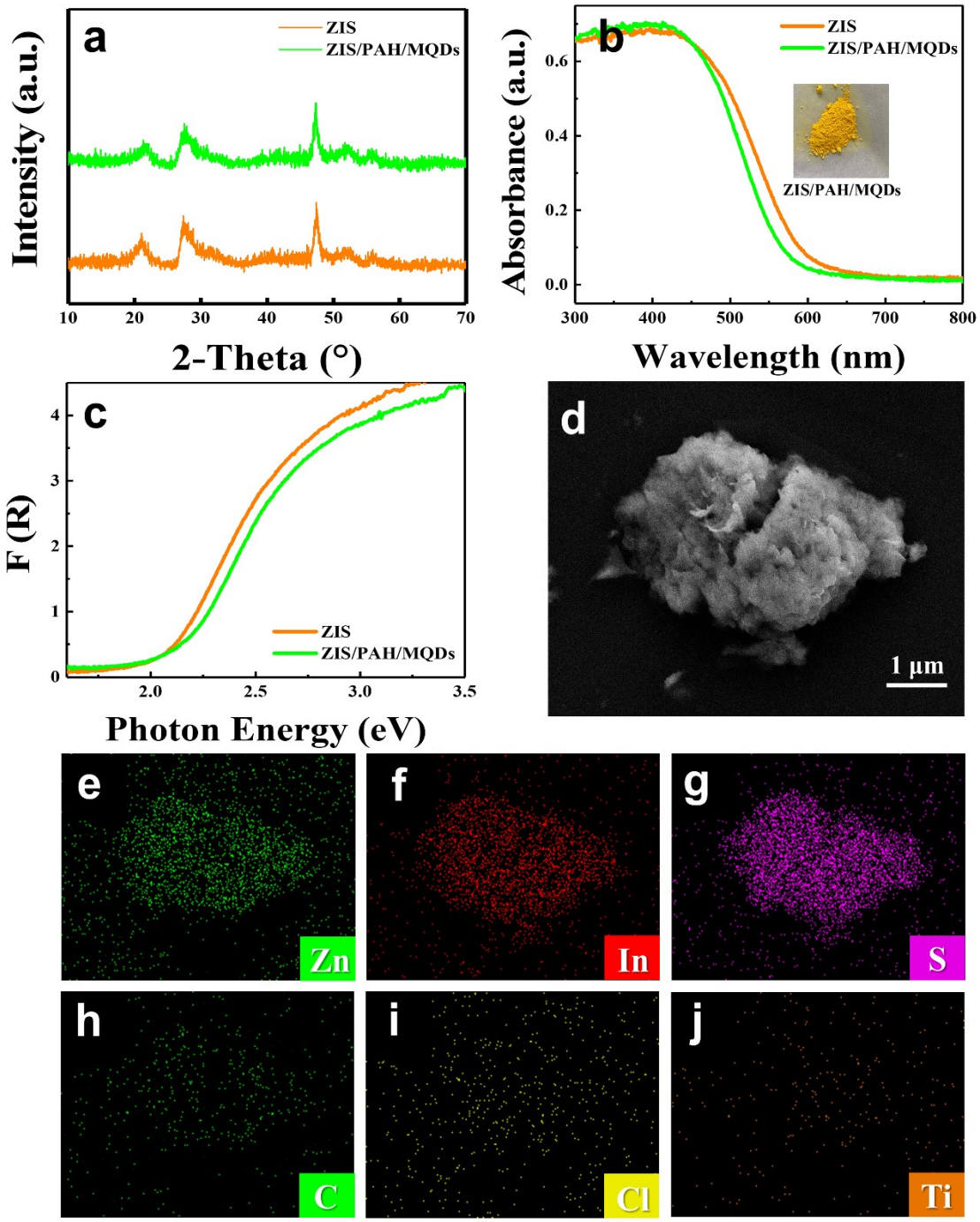

Fig. S26. (a) XRD patterns of blank ZIS and ZIS/PAH/MQDs; (b) DRS spectra of ZIS and ZIS/PAH/MQDs with (c) transformed plots calculated based on the Kubelka–Munk function vs. the energy of light; (d) FESEM image and (e-j) elemental mapping result of ZIS/PAH/MQDs.

Note: XRD pattern of ZIS/PAH/MQDs (**Fig. S26a**) shows the hexagonal phase $ZnIn_2S_4$ (JCPDS No. 65-2023) [S1], similar to that of pure $ZnIn_2S_4$. As displayed in **Fig. S26(b & c)**, $ZnIn_2S_4$ and ZIS/PAH/MQDs exhibit the similar absorption edge, indicating both PAH and MQDs deposition does not influence the optical property of $ZnIn_2S_4$ NSs. Elemental mapping result of ZIS/PAH/MQDs in **Fig. S26(e-j)** demonstrates the uniform distribution patterns of Zn, In, S, C, Cl and Ti signals.

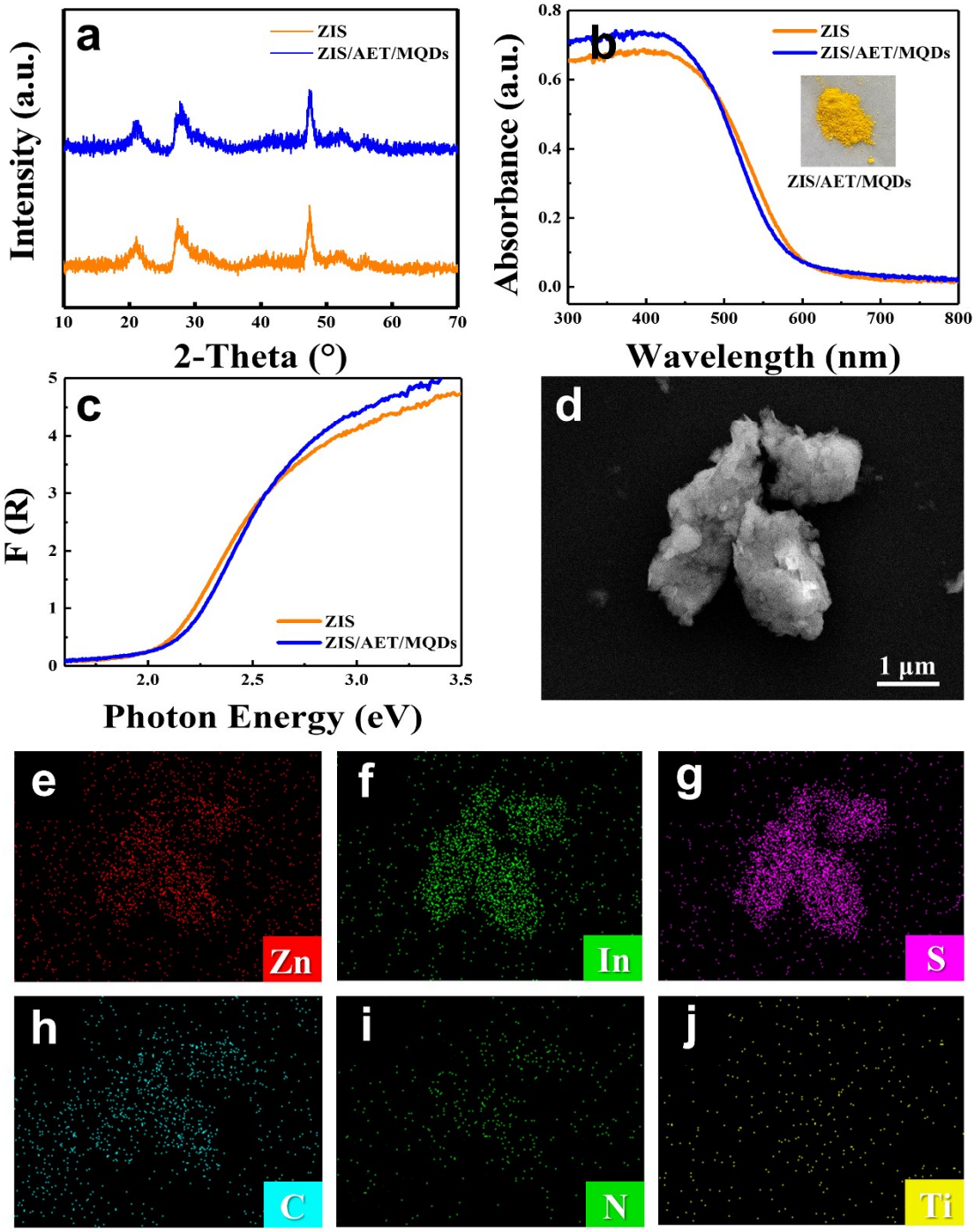

Fig. S27. (a) XRD patterns of blank ZIS and ZIS/AET/MQDs; (b) DRS spectra of ZIS and ZIS/AET/MQDs with (c) transformed plots calculated based on the Kubelka–Munk function vs. the energy of light; (d) FESEM image and (e-j) elemental mapping result of ZIS/AET/MQDs.

Note: XRD pattern of ZIS/AET/MQDs (**Fig. S27a**) shows the hexagonal phase $ZnIn_2S_4$ (JCPDS No. 65-2023) [S1], similar to that of pure $ZnIn_2S_4$. As displayed in **Fig. S27(b & c)**, $ZnIn_2S_4$ and ZIS/AET/MQDs exhibit the similar absorption edge, indicating both AET and MQDs deposition does not influence the optical property of $ZnIn_2S_4$ NSs. Elemental mapping result of ZIS/AET/MQDs in **Fig. S27(e-j)** demonstrates the uniform distribution patterns of Zn, In, S, C, N and Ti signals.

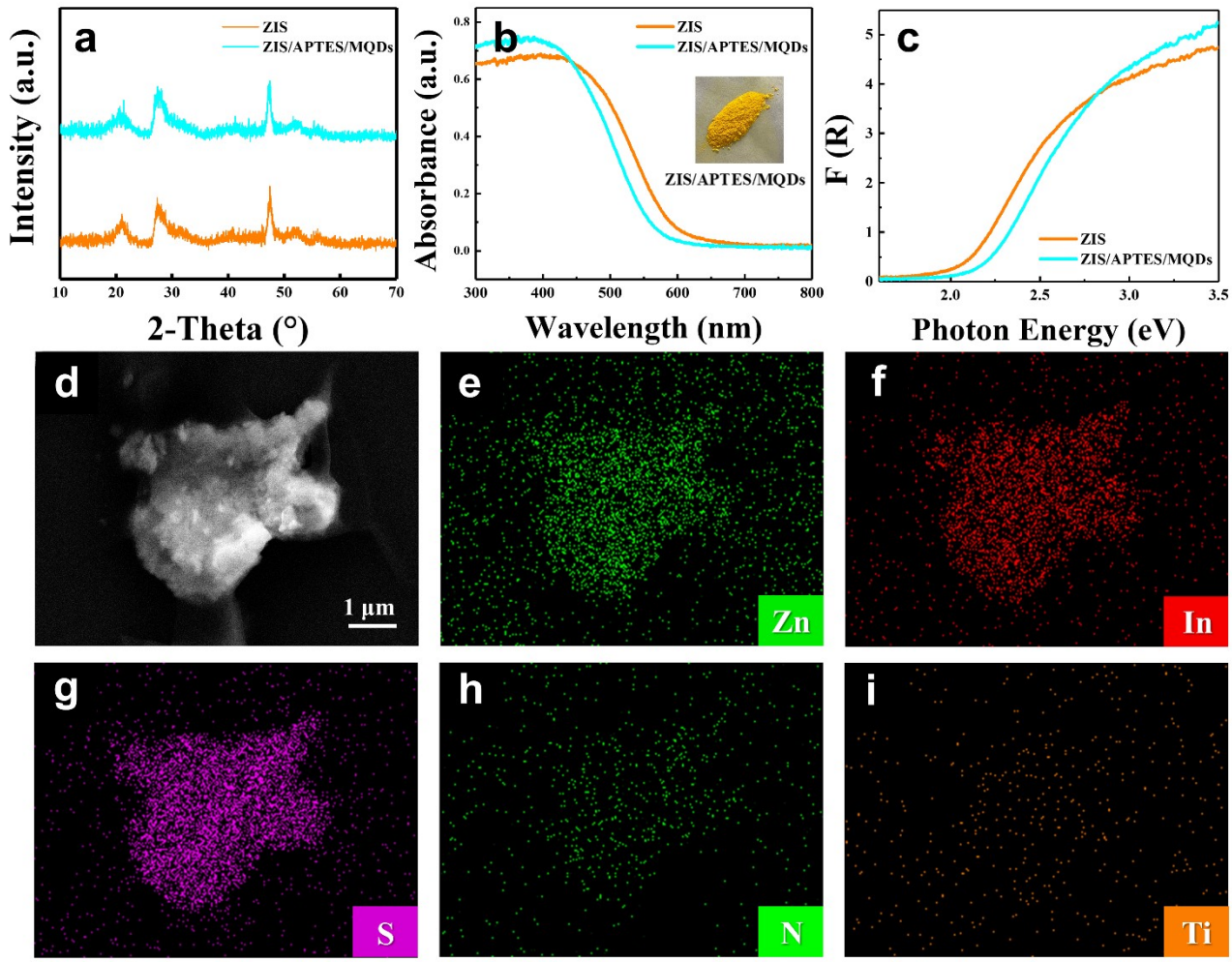

Fig. S28. (a) XRD patterns of blank ZIS and ZIS/APTES/MQDs; (b) DRS spectra of ZIS and ZIS/APTES/MQDs with (c) transformed plots calculated based on the Kubelka–Munk function vs. the energy of light; (d) FESEM image and (e-i) elemental mapping result of ZIS/APTES/MQDs.

Note: XRD pattern of ZIS/APTES/MQDs (**Fig. S28a**) shows the hexagonal phase $ZnIn_2S_4$ (JCPDS No. 65-2023), [S1] similar to that of pure $ZnIn_2S_4$. As displayed in **Fig. S28(b & c)**, $ZnIn_2S_4$ and ZIS/APTES/MQDs exhibit the similar absorption edge, indicating both APTES and MQDs deposition does not influence the optical property of $ZnIn_2S_4$ NSs. Elemental mapping result of ZIS/APTES/MQDs in **Fig. S28(e-i)** demonstrates the uniform distribution patterns of Zn, In, S, N and Ti signals.

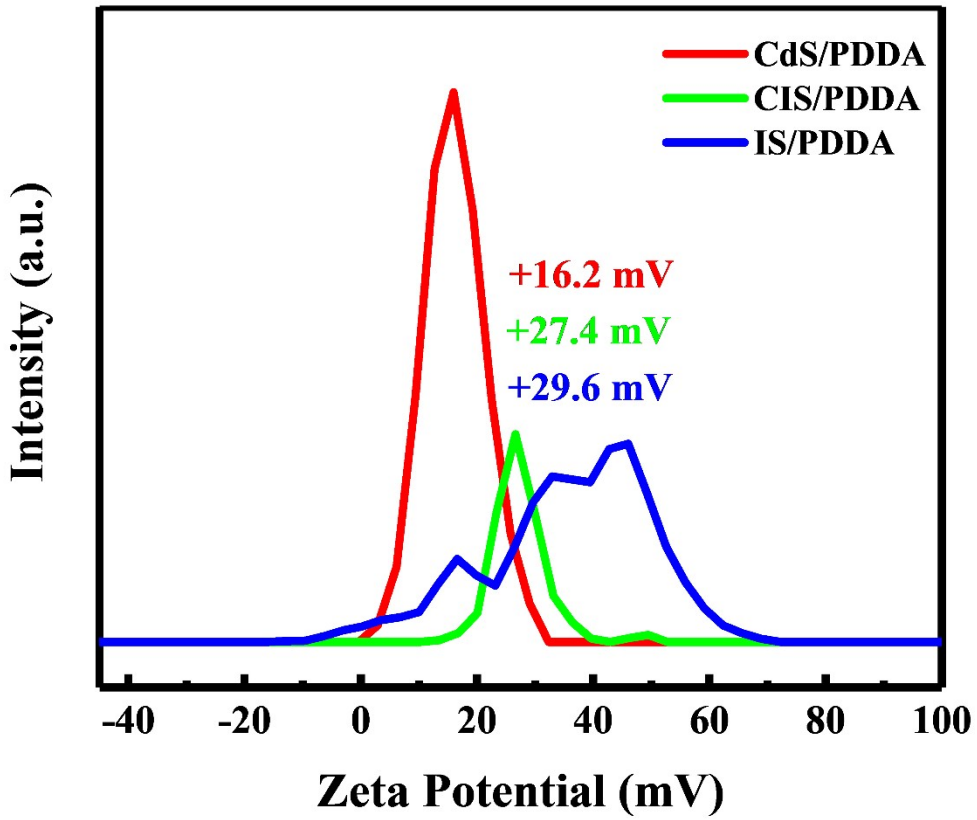

Fig. S29. Zeta potentials of CdS/PDDA, CIS/PDDA and IS/PDDA

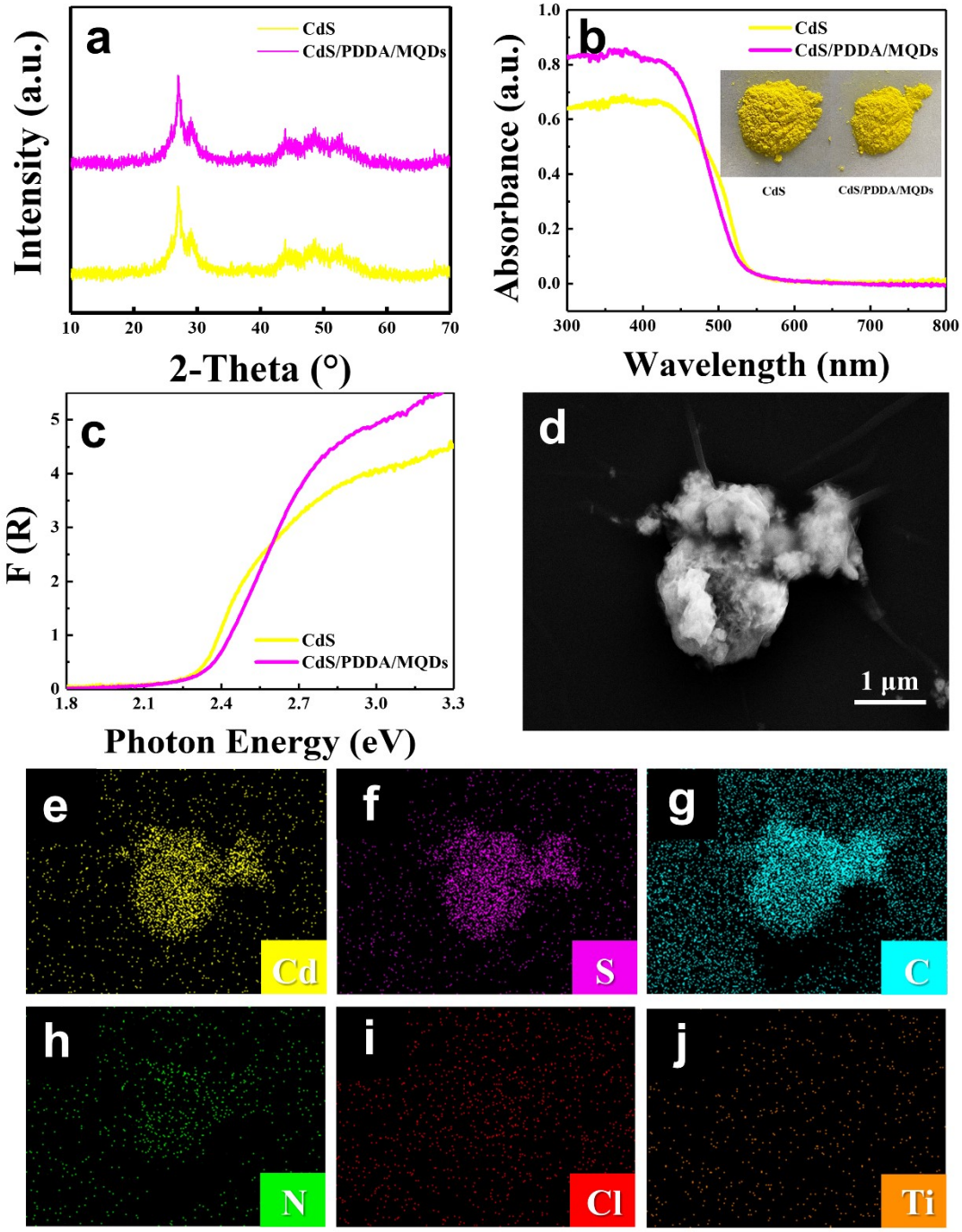

Fig. S30. (a) XRD patterns of blank CdS and CdS/PDDA/MQDs; (b) DRS spectra of CdS and CdS/PDDA/MQDs with (c) transformed plots calculated based on the Kubelka–Munk function vs. the energy of light; (d) FESEM image and (e-h) elemental mapping result of CdS/PDDA/MQDs,

Note: XRD pattern of CdS/PDDA/MQDs (**Fig. S30a**) shows the hexagonal phase CdS (JCPDS No. 77-2306) [S2], similar to that of pure CdS. As displayed in **Fig. S30(b & c)**, CdS and CdS/PDDA/MQDs exhibit the similar absorption edge, indicating both PDDA and MQDs deposition does not influence the optical property of CdS NSs. Elemental mapping result of ZIS/APTES/MQDs in **Fig. S30(e-j)** of Cd, S, C, N, Cl and Ti signals.

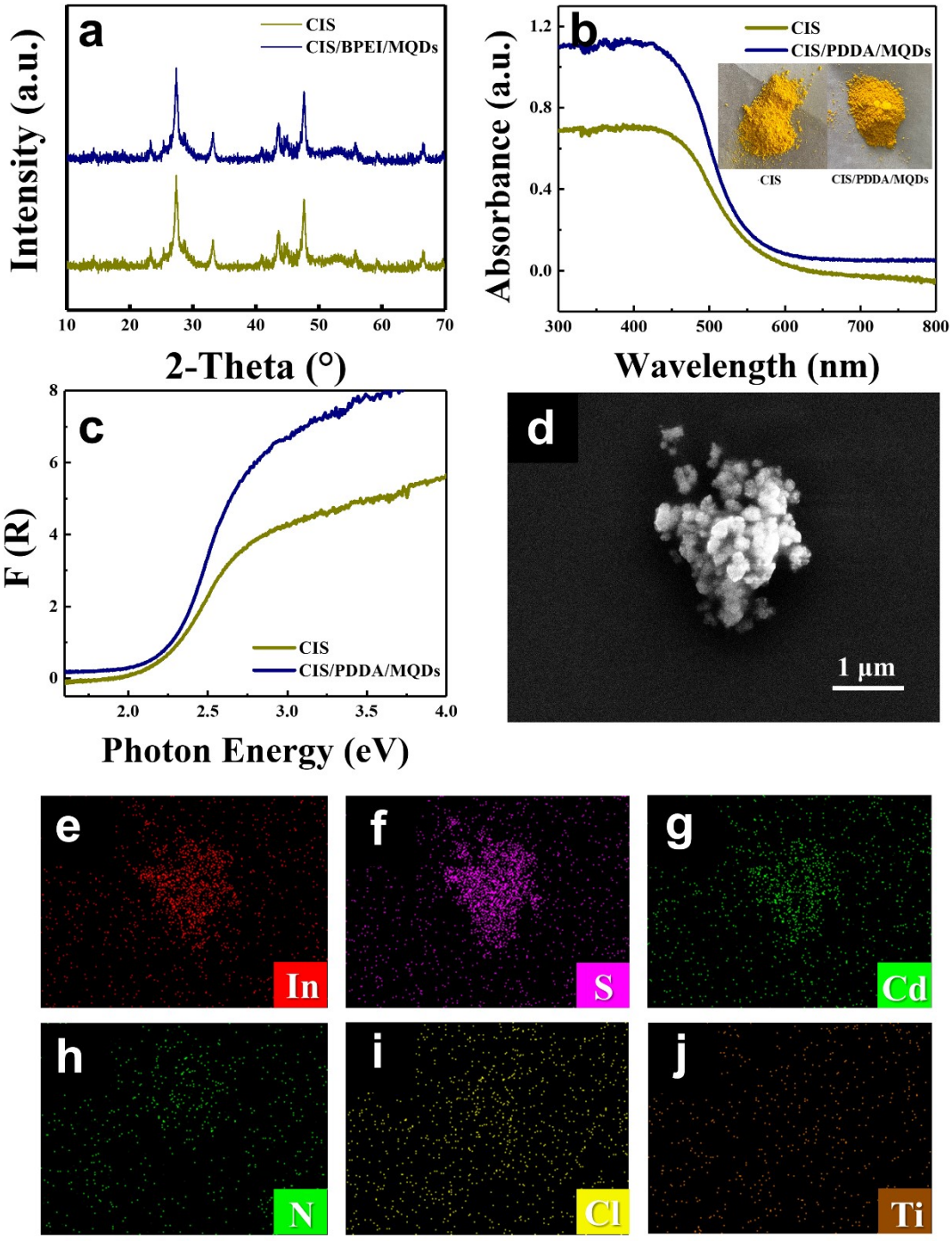

Fig. S31. (a) XRD patterns of blank CIS and CIS/PDDA/MQDs; (b) DRS spectra of CIS and CIS/PDDA/MQDs with (c) transformed plots calculated based on the Kubelka–Munk function vs. the energy of light; (d) FESEM image and (e-j) elemental mapping result of CIS/PDDA/MQDs, .

Note: XRD pattern of CIS/PDDA/MQDs (**Fig. S31a**) shows the cubic phase CIS (JCPDS No. 27-0060) [S3],similar to pure CIS. As displayed in **Fig. S31(b & c)**, CIS and CIS/PDDA/MQDs exhibit the similar absorption edge, indicating both PDDA and MQDs deposition does not influence the optical property of CIS NSs. Elemental mapping result of CIS/PDDA/MQDs in **Fig. S31(e-j)** demonstrates the uniform distribution patterns of Cd, In, S, N, Cl and Ti signals.

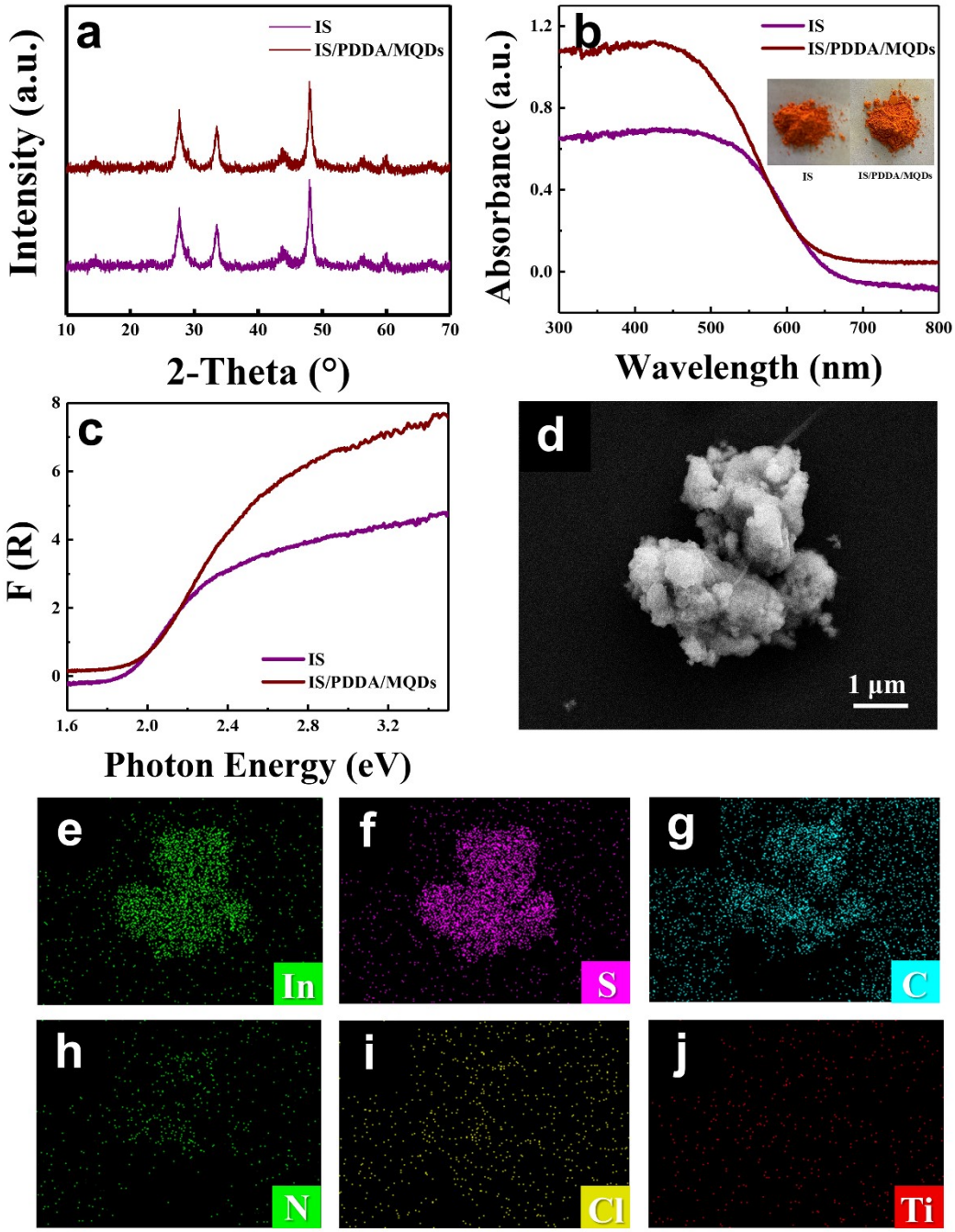

Fig. S32. (a) XRD patterns of blank IS and IS/PDDA/MQDs heterostructure; (b) DRS spectra of IS and IS/PDDA/MQDs heterostructure with (c) transformed plots calculated based on the Kubelka–Munk function vs. the energy of light; (d) FESEM image and (e-j) elemental mapping results of IS/PDDA/MQDs.

Note: XRD pattern of IS/PDDA/MQDs (**Fig. S32a**) shows the cubic phase IS ((JCPDS No. 65-0459) [S3], similar to pure IS. As displayed in **Fig. S32(b & c)**, IS and IS/PDDA/MQDs exhibit the similar absorption edge, indicating both PDDA and MQDs deposition does not influence the optical property of IS NSs. Elemental mapping result of IS/PDDA/MQDs in **Fig. S32(e-j)** demonstrates the uniform distribution patterns of In, S, C, N, Cl and Ti signals.

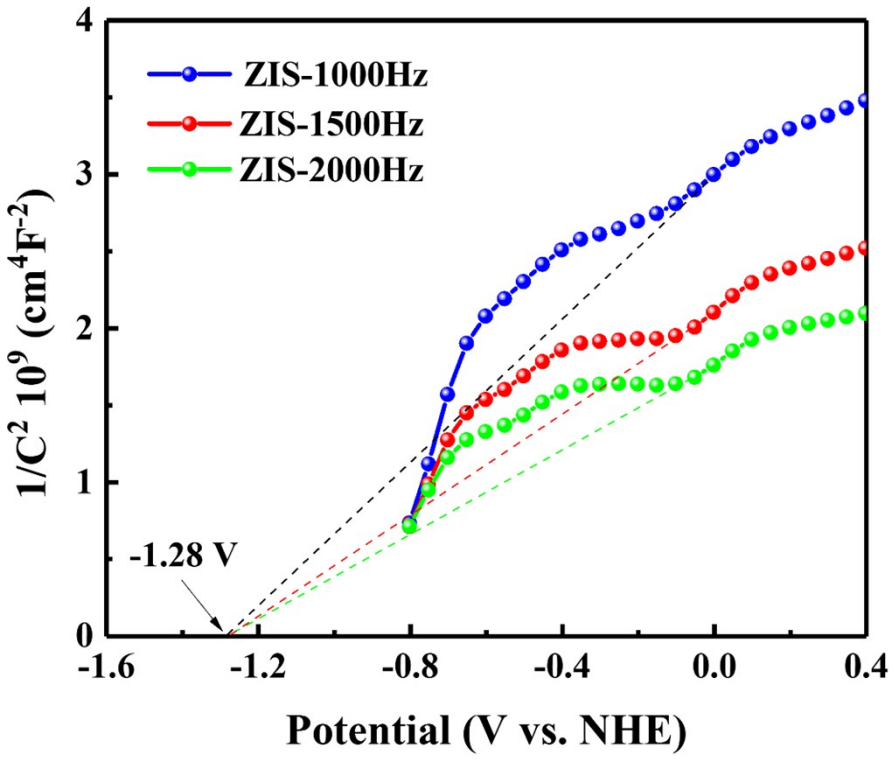

Fig. S33. Mott-Schottky plots of ZIS NSs probed under different frequencies.

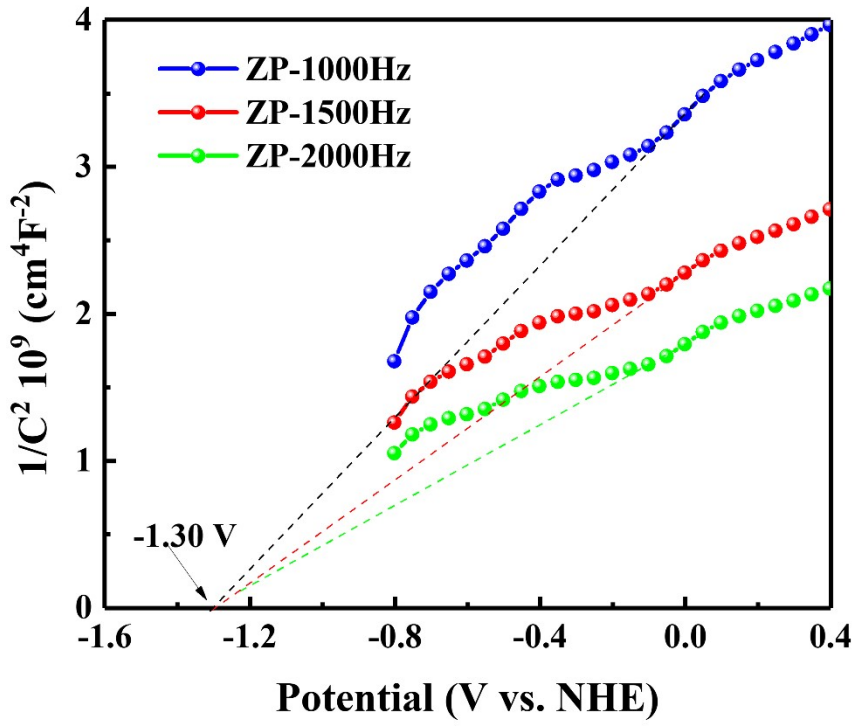

Fig. S34. Mott-Schottky plots of ZP NSs probed under different frequencies.

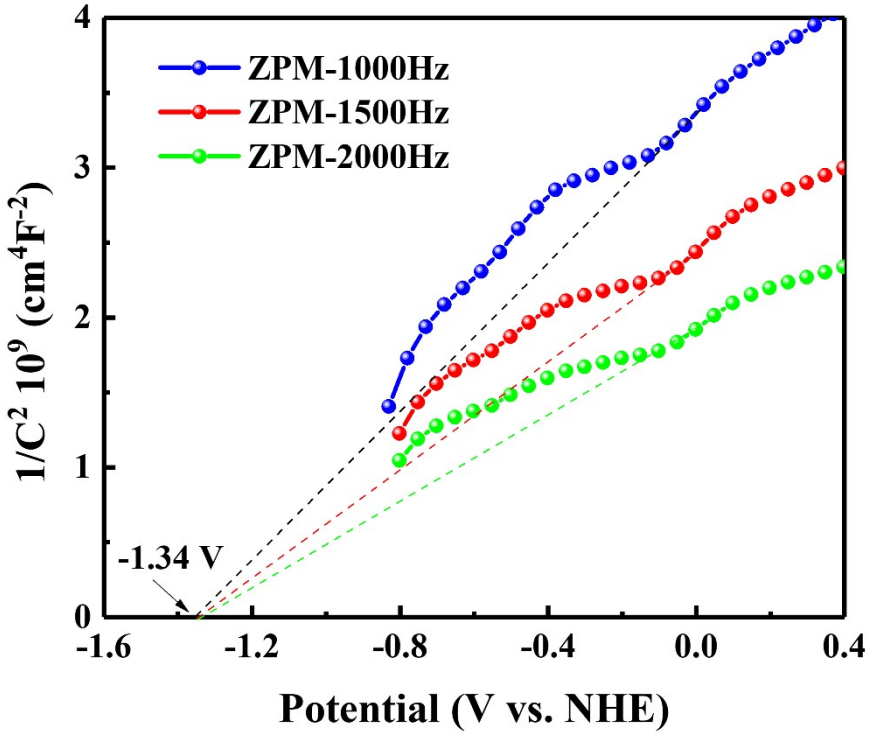

Fig. S35. Mott-Schottky plots of ZP NSs probed under different frequencies.

Note: Flat band position (V_{fb}) can be determined by Mott-Schottky plots probed under different frequencies. Apparently, intersection point does not depend on the frequency, and V_{fb} potentials of ZIS, ZP and ZPM are approximately determined as -1.28 V, -1.30 V, and -1.34 V vs. NHE.

Table S1. Functional groups vs. wavenumber for different samples.

Wavenumber (cm^{-1})	Vibration mode	Functional groups or Chemical bonds
3430	υ_{O-H}	N-H
2850 & 2923	υ_{C-H}	$-CH_2-$
1620	υ_{O-H}	C=O
1380	δ_{C-H}	$-CH_3$
617	Ti-C	Ti_3C_2

Table S2. Specific surface area, pore volume and pore size of ZIS NSs, ZP, and ZPM.

Samples	S_{BET} (m^2/g)[a]	Total pore volume (cm^3/g)[b]	Average pore size (nm)[c]
ZIS	51.7358	0.052424	23.110
ZP	23.0015	0.045723	24.433
ZPM	29.7899	0.043045	28.899

Table S3. Chemical bond species vs. B.E. for different samples.

Element	ZIS NSs	ZPM	Chemical Bond Species
Zn $2p_{3/2}$	1022.18 eV	1022.07 eV	Zn^{2+}
Zn $2p_{1/2}$	1045.18 eV	1045.27 eV	Zn^{2+}
In $3d_{5/2}$	445.14 eV	445.35 eV	In^{3+}
In $3d_{3/2}$	452.68 eV	452.46 eV	In^{3+}
S $2p_{3/2}$	161.83 eV	161.96 eV	S^{2-}
S $2p_{1/2}$	163.13 eV	163.17 eV	S^{2-}
C 1s	284.80 eV	248.80 eV	$C\text{-}C^{-}$
C 1s	286.50 eV	286.66eV	C-N
C 1s	288.46 eV	288.31eV	C=O
N 1s	400.13 eV	400.14 eV	Primary amine
N 1s	Not detected	402.59 eV	NH_4^+
Ti 2p	Not detected	461.88 eV	Ti-C

Table S4. Photoactivities of different samples toward reduction of a series of nitroaromatic compounds under visible light irradiation (λ>420 nm).

Number	Substrate	Conversion (%)			
		ZIS NSs	ZP	ZPM	ZM
a	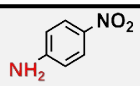	23.05	41.38	93.64	41.30
b		9.65	27.11	54.83	32.22
c	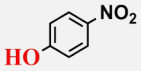	16.98	30.06	62.14	36.70
d		20.61	47.48	67.14	30.34
f	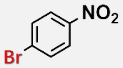	26.53	54.74	72.59	58.61
g	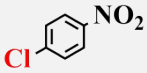	25.27	55.66	73.01	47.61
h	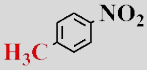	32.31	42.17	61.39	37.5
i	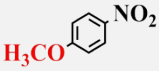	30.66	51.54	76.33	53.11
j		19.85	35.64	55.30	36.58

Table S5. Photoactivities of different samples toward 4-NA photoreduction under visible light irradiation (λ>420 nm).

Number	Sample	Irradiation time (min)	Conversion (%)
1	ZIS	25	23.05
2	ZIS/BPEI	25	76.67
3	ZIS/BPEI/MQDs	25	97.73
4	ZIS/PAH	25	58.24
5	ZIS/PAH/MQDs	25	89.68
6	ZIS/AET	25	64.40
7	ZIS/AET/MQDs	25	91.33
8	CdS	5	42.99
9	CdS/PDDA	5	86
10	CdS/PDDA/MQDs	5	89.88
11	CIS	10	41.44
12	CIS/PDDA	10	60.24
12	CIS/PDDA/MQDs	10	80.12
13	IS	10	32.14
14	IS/PDDA	10	38.17
15	IS/PDDA/MQDs	10	59.56

Table S6. Fitted EIS results of different samples based on the equivalent circuit

Sample	Rs / ohm	Rct / ohm	CPE/(F • cm^{-2})
ZIS	17.81	9187	0.0001210
ZP	16.4	7365	0.0000872
ZPM	15.99	5202	0.0000569

References

S1. Yang, M. -Q.; Xu, Y. J.; Lu, W. H.; Zeng, K. Y.; Zhu, H.; Xu, Q. H.; Ho, G. W. Self-surface charge exfoliation and electrostatically coordinated 2D hetero-layered hybrids. *Nat. Commun.* 2017, 8, 14224.

S2. Xie, X. Q.; Zhang, N.; Tang, Z. R.; Anpo, M.; Xu, Y.- J. $Ti_3C_2T_x$ MXene as a Janus cocatalyst for concurrent promoted photoactivity and inhibited photocorrosion. *Appl. Catal., B* 2018, 237, 43-49.

S3. Mo, Q. L.; Lin, X.; Wei, Z. Q.; Dai, X. C.; Hou, S.; Li, T.; Xiao, F. -X. All-in-one: branched macromolecule-protected metal nanocrystals as integrated charge separation/motion centers for enhanced photocatalytic selective organic transformations. *J. Mater. Chem. A* 2020, 8, 16392-16404.

S4. Xue, Q.; Zhang, H. J.; Zhu, M. S.; Pei, Z. X.; Li, H. F.; Wang, Z. F.; Huang, Y.; Huang, Y.; Deng, Q. H.; Zhou, J.; Du, S. Y.; Huang, Q.; Zhi, C. Y. Photoluminescent Ti_3C_2 MXene Quantum Dots for Multicolor Cellular Imaging. *Adv. Mater.* **2017**, *29*, 1604847.